

Fast Active Monocular Distance Estimation from Time-to-Contact

Levi Burner*, Nitin J. Sanket, Cornelia Fermüller, Yiannis Aloimonos

Perception and Robotics Group, University of Maryland Institute for Advanced Computer Studies
University of Maryland, College Park

Abstract

Distance estimation is fundamental for a variety of robotic applications including navigation, manipulation and planning. Inspired by the mammal’s visual system, which gazes at specific objects (active fixation), and estimates when the object will reach it (time-to-contact), we develop a novel constraint between time-to-contact, acceleration, and distance that we call the τ -constraint. It allows an active monocular camera to estimate depth using time-to-contact and inertial measurements (linear accelerations and angular velocities) within a window of time.

Our work differs from other approaches by focusing on patches instead of feature points. This is, because the change in the patch area determines the time-to-contact directly. The result enables efficient estimation of distance while using only a small portion of the image, leading to a large speedup.

We successfully validate the proposed τ -constraint in the application of estimating camera position with a monocular grayscale camera and an Inertial Measurement Unit (IMU). Specifically, we test our method on different real-world planar objects over trajectories 8-40 seconds in duration and 7-35 meters long. Our method achieves 8.5 cm Average Trajectory Error (ATE) while the popular Visual-Inertial Odometry methods VINS-Mono and ROVIO achieve 12.2 and 16.9 cm ATE respectively. Additionally, our implementation runs $27\times$ faster than VINS-Mono’s and $6.8\times$ faster than ROVIO’s. We believe these results indicate the τ -constraints potential to be the basis of robust, sophisticated algorithms for a multitude of applications involving an active camera and an IMU.

1. Introduction

Early researchers in computer vision were fascinated by living being’s ability to control their movement in order to gather information about their environment. The process was named “Active Perception” [1, 3, 6, 11], and numerous

*Corresponding author. The support of the NSF under awards DGE-1632976 and OISE 2020624 is gratefully acknowledged.

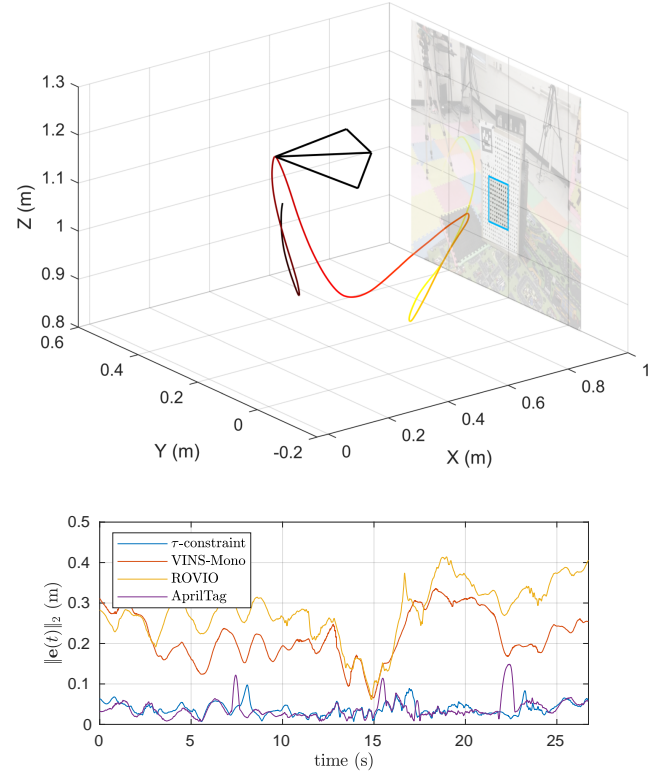


Figure 1. Top: Five seconds of sequence 9’s camera trajectory along with the fixated scene patch used to estimate 3D distance using a monocular camera and an IMU. Bottom: l_2 error for Seq. 9 of our method compared to VINS-Mono, ROVIO, and AprilTag 3. Averaged over all sequences, our method is 50% and 30% more accurate and $27\times$ and $6.8\times$ faster than VINS-Mono and ROVIO while also using only a small portion of the image (initially 2.5%). Time is color coded with the hot colormap.

mechanisms for exploiting activeness were developed over the past thirty years. In [18], four forms of activeness are described, three of which require physical movement. It is in this sense, that we use the word “active”, e.g. to mean “movement at will” or “moving” rather than active illumination like RGB-D cameras. The goal of all forms is to

reduce the computational load on the system by distributing the task at hand between action and perception [29].

Because, active vision systems are usually moving in some way, they must accelerate to produce changes to this movement. Despite this, utilizing observer acceleration (measured using an Inertial Measurement Unit or IMU) to facilitate visual computations has not received much attention in the Active Vision literature. To fill this gap, we introduce a new mathematical constraint relating (a) time-to-contact (τ) (the ratio of camera velocity to scene distance) with (b) scene depth and (c) observer acceleration. This constraint makes it possible for an active monocular camera to estimate scene depth by accelerating in any direction. We call this the τ -constraint.

We demonstrate the utility of the constraint in a series of experiments involving fixation on a single object (i.e, tracking) while the active (moving) monocular camera is accelerating. Fixation is key to the method’s efficiency because it can ignore most of the incoming pixels. Such object-centered representations have been argued to be useful for a wide variety of tasks ranging from manipulation to navigation [4, 6, 12].

The key concept of fusing inertial measurements with camera observations has been extensively studied in the fields of Structure from Motion (SfM) and Simultaneous Localization and Mapping (SLAM). Traditionally, this fusion has been achieved in Visual Inertial Odometry (VIO) frameworks using a series of Bayesian filters or Factor graphs [17, 30].

It is important to stress that our implementation is not a fully-functional VIO implementation, and is only intended to empirically demonstrate the efficacy of the τ -constraint. Nevertheless, it naturally results in a trajectory estimate. For this reason, we compare our method with the popular state-of-the-art VIO methods VINS-Mono and ROVIO as well as the fiducial marker based pose estimation method, AprilTag 3 [20, 27]. To provide a firm grounding to our results, we also compare our results with millimeter accurate ground truth from a Vicon motion capture system.

We formally define our problem statement next along with a summary of our contributions.

1.1. Problem Definition and Contributions

We solve the mathematical problem of estimating distance to a scene patch, using time-to-contact, and acceleration measurements in closed form.

To test our result, we implement a method of estimating time-to-contact from the change of a patch’s area in the image plane and couple it with acceleration measurements through the novel τ -constraint.

A list of our contributions are given below:

- A closed form solution for estimating the 3D position

of the camera given a short history of time-to-contact and acceleration.

- A computationally efficient method of 3D position estimation utilizing the τ -constraint, which demonstrates viability with inexpensive sensors.
- Comparisons against the popular VIO methods, VINS-Mono and ROVIO, as well as the fiducial marker based posed estimation method, AprilTag 3, to show the efficacy of the novel constraint in a real-world setting.

We believe that our constraint will open doors for a multitude of applications using an active camera and an IMU.

2. Related Work

A multitude of prior works from both the computer vision and robotics literature deal with time-to-contact and the fusion of camera and IMU measurements to obtain relative camera pose (odometry). However, to the best of our knowledge, none of these works provided a closed form solution for the estimation of distance from time-to-contact and inertial measurements.

Time-to-contact

One of the earliest works to discuss how time-to-contact τ can be used in control tasks is [22]. It provides a mathematical analysis on how time-to-contact, τ , could be used by humans driving a vehicle to judge when to start braking and how to control ongoing braking. The idea was further developed to create a “General Tau Theory” to understand how human’s might perform control for a wide variety of tasks [23].

Because of its intuitive formulation, τ has also been the subject of many studies in computer vision and robotics. [31] showed how to land a spacecraft using event cameras by computing τ from the divergence of optical flow. [32] fuses information from a depth camera and τ to compute “time-to-impact” which can in-turn be used to dodge dynamic obstacles without prior knowledge of scene geometry or obstacles. In robotics, most methods that perform optical flow based control use initial height estimates either implicitly or explicitly, as remarked in [15]. To this end, [15] proposed to fuse control effort with flow divergence or τ with an extended Kalman filter in order to recover depth. Another strategy exploits the instability that manifests at certain heights when performing τ control with fixed gain feedback to estimate depth [10]. In the context of self driving cars, BinaryTTC [2] proposed a network to predict per-pixel τ with arbitrarily fine quantization to achieve real-time performance. Finally, it is important to note that τ can be efficiently computed when the scene under consideration is planar in nature [16].

Visual Inertial Odometry (VIO)

One of the earliest works [26] for real-time VIO fused sparse feature tracks with IMU measurements using a Multi-State Constraint Kalman Filter. The pipeline was then made more robust by ROVIO [8] which used patch tracking and enforced photometric consistency with IMU measurements using an Iterative Extended Kalman Filter. ROVIO required robust initialization, accurate intrinsic and extrinsics, and IMU calibration for accurate odometry estimation. To this end, VINS-Mono [27] introduced a nonlinear optimization based sliding window estimator with pre-integrated IMU factors and an initialization-free formulation. Note that in the context of classical VIO, *direct* methods operate by directly incorporating constraints on pixel intensities into the optimization formulation whereas *indirect* methods utilize features and enforce geometric constraints defined on these features from multiple views. Fundamental to these methods is the underlying proof that tracked points and inertial measurements allow pose to be recovered in closed form [24, 25]. VIO is called *loosely-coupled* if both the sensors are used to predict pose separately. On the other hand, *tightly-coupled* formulations obtain pose by combining measurements from both sensors directly in an optimization problem.

Recent deep learning based VIO methods have achieved better accuracy than classical approaches. VINet [9] presented the first supervised method to estimate odometry using a CNN + LSTM architecture by combining visual and inertial data. This was later improved by DeepVIO [13] using supervision from a stereo camera for better robustness. The limiting factor of these approaches is a lack of speed and generalization across various compute platforms [28]. As will be shown, the τ -constraint can be formulated as a loss, which may be interesting for future work in deep VIO.

Our classical implementation is based on a tightly coupled optimization of the τ -constraint with respect to acceleration and time-to-contact. Time-to-contact is determined from a directly formulated patch tracker. The results are combined with a linear observer to limit the effects of noise.

3. Derivation of the τ -constraint

This work incorporates two concepts: time-to-contact and visual-inertial fusion. We mathematically derive a formulation for the relation between τ at a scene point, the depth at that scene point, and acceleration of the camera, which we call the τ -constraint. This allows us to estimate metric distance and relative camera pose an order of magnitude faster than standard VIO methods by ignoring pixels outside of a local neighborhood of the scene point.

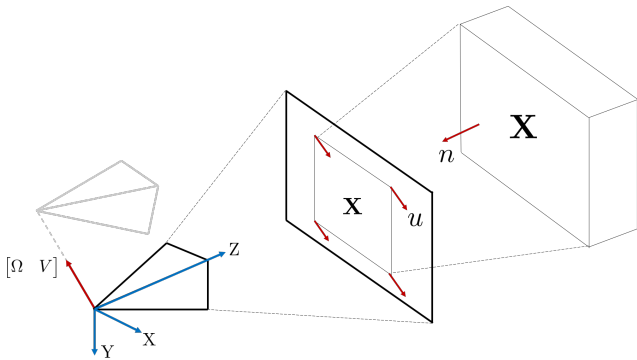


Figure 2. Definition of camera coordinates for a scene point \mathbf{X} being imaged at image point \mathbf{x} . The moving camera “perceives” the movement of the scene point as optical flow \mathbf{u} .

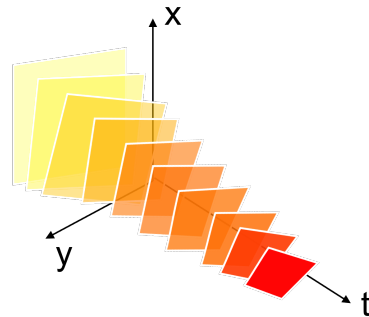


Figure 3. The patch being tracked over time changes in shape and location and is modelled by an affine transformation. Time is color coded as yellow to red.

3.1. Organization

Below, we derive the τ -constraint starting from an affine homography of a scene patch. We show how the affine homography determines the planar flow and then rearrange the planar flow’s parameters to find time-to-contact, and its generalization as frequency-of-contact. Once these preliminaries are in place, the τ -constraint is stated and proven.

It is important to note that time-to-contact can be estimated with methods other than planar flow and thus the τ -constraint stands on its own. However, building up to the statement of the τ -constraint through planar flow is more illuminating.

3.2. Estimating Time-to-Contact with Affine Flow

As illustrated in Fig. 2, the optical flow $\mathbf{u}(t)$ at an image location $\mathbf{x} = [x \ y \ 1]^T$ is given as

$$\mathbf{u}_{\mathbf{x}} = K \frac{\dot{\mathbf{X}}_{\mathbf{x}}}{Z_{\mathbf{x}}} - K \frac{\dot{Z}_{\mathbf{x}}}{Z_{\mathbf{x}}} \mathbf{x}, \quad (1)$$

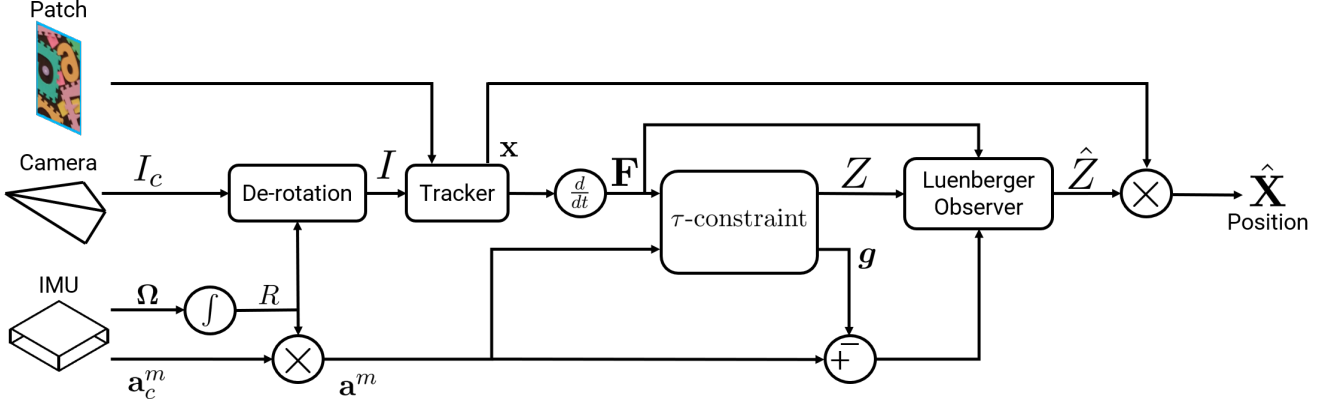


Figure 4. System overview of our method to estimate camera position using the τ -constraint.

where $\dot{\mathbf{X}}_{\mathbf{x}}$ is the velocity of the scene point corresponding to pixel \mathbf{x} in the camera coordinate frame.

Without loss of generality, let us assume the camera is calibrated so that the focal length is of unit length and the projection matrix is $K = \mathbb{I}_{3 \times 3}$.

Under rigid motion, $\dot{\mathbf{X}}_{\mathbf{x}}$ is related to the camera translational velocity \mathbf{V} and rotational velocity Ω as $\dot{\mathbf{X}}_{\mathbf{x}} = -\Omega \times \mathbf{X}_{\mathbf{x}} - \mathbf{V}$. Due to de-rotation from IMU measurements (rotation compensated image frames) we proceed with the assumption that $\Omega = 0$ and without loss of generality refer to $\dot{\mathbf{X}}_{\mathbf{x}}$ as $\dot{\mathbf{X}}$.

Let us assume that the scene patch we are looking at is planar. A simple formulation to model the change of patch area over time is the affine homography transformation. Because the affine homography is linear, its derivative defines an affine flow field. Thus, we can model the optical flow of the rotation compensated image patch corresponding to the planar scene patch as

$$\mathbf{u}_{\mathbf{x}} = A\mathbf{x} = \begin{bmatrix} a_1 & a_2 & a_3 \\ a_4 & a_5 & a_6 \\ 0 & 0 & 0 \end{bmatrix} \mathbf{x}, \quad (2)$$

where $A(t)$ is a time-varying affine transformation of the homogeneous image location \mathbf{x} .

Let us derive A in terms of physical quantities. Let the scene points $\mathbf{X}_{\mathbf{x}}$ lie on the plane $1/Z_{\mathbf{x}} = [n_x, n_y, n_z] [X_{\mathbf{x}}/Z_{\mathbf{x}}, Y_{\mathbf{x}}/Z_{\mathbf{x}}, 1]^T = \mathbf{n}^T \mathbf{x}$. By substituting this expression for $1/Z_{\mathbf{x}}$ into equation (2), we obtain:

$$\begin{aligned} \mathbf{u}_{\mathbf{x}} &= [\dot{\mathbf{X}} - \dot{Z}\mathbf{x}] \mathbf{n}^T \mathbf{x} \\ &= \dot{\mathbf{X}} \mathbf{n}^T \mathbf{x} - \dot{Z} n_z \mathbf{x} - \underbrace{\dot{Z} \mathbf{x} (n_x x + n_y y)}_{\gamma} \\ &= \underbrace{\begin{bmatrix} \dot{X} n_x - \dot{Z} n_z & \dot{X} n_y & \dot{X} n_z \\ \dot{Y} n_x & \dot{Y} n_y - \dot{Z} n_z & \dot{Y} n_z \\ 0 & 0 & 0 \end{bmatrix}}_{A(t):=} \mathbf{x} - \begin{bmatrix} \gamma_x \\ \gamma_y \\ 0 \end{bmatrix} \end{aligned} \quad (3)$$

The assumption of an affine homography, as used by the tracker, implies an affine flow-field. Thus, γ will always be measured as zero, i.e., the quadratic terms in the flow field are not known.

By rearranging the components of A to recover $\dot{\mathbf{X}} \mathbf{n}^T$ we can then write $\dot{\mathbf{X}}/Z_{\mathbf{x}}$ in terms of the affine flow parameters A and an image location \mathbf{x} . Let $\eta := ((a_4 a_3 / a_6) - a_1)$, then

$$\frac{\dot{\mathbf{X}}}{Z_{\mathbf{x}}} = \begin{bmatrix} a_4 a_3 / a_6 & a_2 & a_3 \\ a_4 & a_2 a_6 / a_3 & a_6 \\ \eta(a_4 / a_6) & \eta(a_2 / a_3) & \eta \end{bmatrix} \mathbf{x}. \quad (4)$$

The third element of $\dot{\mathbf{X}}/Z_{\mathbf{x}}$ is the inverse of time-to-contact. Thus, by tracking a patch by an affine homography, we can estimate the affine flow parameters, which determine time-to-contact. Because an affine homography defines the location of every point on the planar scene patch in image space at all times, we assume $\dot{\mathbf{X}}/Z_{\mathbf{x}}$ is defined in reference to a particular scene point in the tracked patch for the rest of the paper.

3.3. Frequency-of-Contact as a Generalization of Time-to-Contact

Now, we define the *frequency-of-contact* as

$$\mathbf{F}(t) := \frac{\dot{\mathbf{X}}(t)}{Z(t)} \quad (5)$$

This is the generalization of time-to-contact to all three dimensions because, time-to-contact τ , is classically defined only for camera Z direction as $\tau(t) := -1/F_z(t)$.

Frequency-of-contact is more often well-defined than time-to-contact because it avoids division by zero when the camera is stationary. $\mathbf{F}(t)$ is ill-defined when $Z(t) = 0$. However, this means that the object is on the image plane and cannot be “seen”. For this reason, and without loss of generality, for the rest of the paper we assume Z is bounded away from zero, i.e., $Z(t) \geq \epsilon > 0 \mid \forall t$.

3.4. The τ -constraint

To allow concise expression of the τ -constraint we define the following quantities and an operator that is the double integral of vectors of functions.

$$\begin{aligned} \mathbf{E}(t) &:= \left[\int_0^t \begin{bmatrix} F_X(\lambda) \\ F_Y(\lambda) \\ \Phi_{F_Z}(\lambda) - 1 \end{bmatrix} \Phi_{F_Z}(\lambda) d\lambda \right] - t\mathbf{F}(0) \\ \Phi_{F_Z}(t) &:= \exp\left(\int_0^t F_Z(\lambda) d\lambda\right) \\ \Delta\{\mathbf{f}\}(t) &:= \int_0^t \left(\int_0^\lambda \mathbf{f}(\lambda_2) d\lambda_2\right) d\lambda \end{aligned} \quad (6)$$

$\mathbf{E}(t)$ equals the position change of the observer due to acceleration divided by the scene depth $Z(0)$. Thus, the magnitude of $\mathbf{E}(t)$ is proportional to the applied acceleration (action) and so we call it the “action’s effect”.

Theorem 3.1 (τ -constraint). *If $\mathbf{F}(t)$ and $\ddot{\mathbf{X}}(t)$ are known for all t in a closed interval and $Z(t) \geq \epsilon > 0$, then the following constraint between depth $Z(0)$, frequency-of-contact \mathbf{F} , and acceleration $\ddot{\mathbf{X}}$ holds for each point on the scene patch.*

$$Z(0)\mathbf{E}(t) = \Delta\{\ddot{\mathbf{X}}\}(t) \quad (7)$$

Proof. The proof proceeds by solving a differential equation whose solution is determined by \mathbf{F} and initial conditions $\mathbf{X}(0)$. Next, $\mathbf{X}(t)$ is expanded using the fundamental theorem of calculus so that \mathbf{X} is determined by $\mathbf{F}(0)$, $\mathbf{X}(0)$, and $\ddot{\mathbf{X}}(0)$. Setting the two expressions for $\mathbf{X}(t)$ equal, leads directly to the τ -constraint.

The definition of frequency-of-contact Eq. (5) can be interpreted as a time-varying linear differential equation.

$$\dot{\mathbf{X}}(t) = \mathbf{F}(t)Z(t) \quad (8)$$

The solution to the above is given by

$$\mathbf{X}(t) = \begin{bmatrix} X(0) \\ Y(0) \\ 0 \end{bmatrix} + \begin{bmatrix} \int_0^t \begin{bmatrix} F_X(\lambda) \\ F_Y(\lambda) \end{bmatrix} \Phi_{F_Z}(\lambda) d\lambda \\ \Phi_{F_Z}(t) \end{bmatrix} Z(0) \quad (9)$$

Now, from the fundamental theorem of calculus, $\mathbf{X}(t)$ is given by

$$\mathbf{X}(t) = \mathbf{X}(0) + \underbrace{t\mathbf{F}(0)Z(0)}_{\dot{\mathbf{X}}(0)} + \underbrace{\int_0^t \left(\int_0^\lambda \ddot{\mathbf{X}}(\lambda_2) d\lambda_2\right) d\lambda}_{\Delta\{\ddot{\mathbf{X}}\}(t)} \quad (10)$$

Eq. (10) satisfies the differential equation defined by \mathbf{F} in Eq. (8), given equal initial conditions. Thus, if the solutions to both systems are unique, they are equal. The complete proof is given in the supplementary material. An intuitive explanation is that \mathbf{X} and its derivatives define all the terms of both of the above expressions for \mathbf{X} . Thus, the solution of Eq. (8) equals Eq. (10).

Setting Eq. (9) equal to Eq. (10) and canceling terms, leads directly to the τ -constraint. \square

4. Fusion of Inertial Measurements and Frequency-of-Contact

To tightly couple IMU measurements and frequency-of-contact from a camera in a sliding window manner, we setup a least squares problem over the τ -constraint. The solution to this problem gives us the current depth of a point in the scene and gravitational acceleration in a fixed frame (camera frame at time $t = 0$, commonly called start-of-service frame).

To re-iterate, as illustrated in Fig. 4, we make our system rotation invariant by integrating the gyroscope measurements Ω to get an estimate of R that rotates the measured acceleration $\mathbf{a}_c^m(t)$ back to a fixed frame $\mathbf{a}^m(t) = R(t)\mathbf{a}_c^m(t)$. The IMU measures the resultant of gravitational acceleration and linear acceleration. Thus, $\mathbf{a}^m(t) = -\ddot{\mathbf{X}} + \mathbf{g}$.

Note that instead of using the IMU measurements, $\ddot{\mathbf{X}}$ could also be determined from the control effort exerted by an active observer (sometimes called “efference copies”).

Let us suppose a history of $\mathbf{a}^m(t)$ and $\mathbf{F}(t)$ are available over a time interval $[0, T]$ and define them to be zero if $t \notin [0, T]$. Similarly, let $\mathbf{1}_{[0, T]}$ be the indicator function over the time window $[0, T]$. Now, without loss of generality, we consider the problem along only the Z axis. The problem can also be solved using motion along the X or Y axis by replacing the subscripts of Z with X or Y . The

fusion from two sources is done through the following optimization problem over the aforementioned time window.

$$\operatorname{argmin}_{Z(0), g_Z} \|E_Z Z(0) + \Delta\{a_Z^m\} + \Delta\{\mathbf{1}_{[0,T]}\}g_Z\|_2^2 \quad (11)$$

Equation (11) is represented by the τ -constraint element in Fig. 4.

4.1. Efficient Computation of Z Distance

Now, we can re-write Eq. 11 as

$$\operatorname{argmin}_y y^T Q y + c^T y \quad (12)$$

$$Q := \begin{bmatrix} \|E_Z\|_2^2 & \langle E_Z, \Delta\{\mathbf{1}_{[0,T]}\} \rangle_2 \\ \langle E_Z, \Delta\{\mathbf{1}_{[0,T]}\} \rangle_2 & \|\Delta\{\mathbf{1}_{[0,T]}\}\|_2^2 \end{bmatrix} \quad (13)$$

$$c := 2 [\langle E_Z, \Delta\{a_Z^m\} \rangle_2 \quad \langle \Delta\{\mathbf{1}_{[0,T]}\}, \Delta\{a_Z^m\} \rangle_2]^T$$

$$y := [Z(0) \quad g_Z]^T.$$

Which, if $Q \succ 0$, has the following unique solution:

$$\begin{bmatrix} Z^*(0) \\ g_Z^* \end{bmatrix} = -\frac{1}{2}Q^{-1}c \quad (14)$$

By the positive semi-definite form of the problem given by Eq. (11), $Q \succeq 0$. Also, the problem is well-posed ($Q \succ 0$) if and only if the acceleration changes during the considered time window. The proof is given in the supplemental material.

Thus, given motion along an axis, scale and gravitational acceleration can be recovered efficiently, by integrating time-to-contact and acceleration measurements and solving a 2-dimensional linear system.

4.2. Filtering of Depth

Now, we extend the above derivation for trajectory estimation. Suppose measurements of $\mathbf{F}(t)$ and $\mathbf{a}^m(t)$ are available over a time window $[t - T, t]$, $T > 0$. Then, as long as the acceleration is not constant in the time window, Eq. (14) can provide estimates of $g_z^*(t)$ and $Z(t)$. Further, an estimate of $\dot{Z}(t)$ can be found by multiplying depth with the frequency of contact in the Z direction, i.e., $\dot{Z}(t) = F_Z(t)Z(t)$.

Then, all three quantities can be fused in a Luenberger observer [14] to obtain smooth trajectory estimates. Let \hat{Z} and $\hat{\dot{Z}}$ be the estimated quantities, then the Luenberger observer for estimating depth and relative speed is

$$\begin{bmatrix} \dot{\hat{Z}}(t) \\ \dot{\hat{\dot{Z}}}(t) \end{bmatrix} = \begin{bmatrix} \hat{\dot{Z}}(t) \\ a_z^m(t) - g_z^*(t) \end{bmatrix} + L \begin{bmatrix} Z(t) - \hat{Z}(t) \\ \dot{Z}(t) - \hat{\dot{Z}}(t) \end{bmatrix} \quad (15)$$

This classic method from the control literature has the property that the estimation error converges to zero globally and exponentially fast [14].

If multiple estimates for $Z(t)$ are available from Eq. (14) due to motion along multiple axis, then results are averaged. In the case that an estimate of $Z(t)$ and $g_z^*(t)$ is not available, due to lack of acceleration change (jerk) that is required by Eq. (14), then dead reckoning based on integration of \dot{Z} is used since time-to-contact is always available during fixation.

Finally, we recover the three dimensional trajectory by multiplying \hat{Z} with the current image location of the point for which time-to-contact is being estimated, e.g.

$$[\hat{X}(t) \quad \hat{Y}(t)]^T := [x(t) \quad y(t)]^T \hat{Z}(t) \quad (16)$$

5. Experiments

We designed an experiment to evaluate the τ -constraint and determine if it is a promising method for future research.

We created ten sequences with five distinct scenes in an indoor setting. Each scene contains a planar object to fixate on as shown in Fig. 1 and Fig. 5. For each scene, two recordings were made, one with an AprilTag and one without.

The sequences were recorded with an Intel® RealSense™ D435i camera using the built-in IMU and the left grayscale camera [19]. We used the grayscale camera because the D435i's IMU is hardware time-stamped to the grayscale imager. The D435i was configured to record at 90 frames per second at 848×480 px. resolution. The IMU was configured to record gyroscope measurements at 400 Hz and the acceleration at 250 Hz.

We tracked the fixated patch using gyroscope measurements for rotation stabilization and by continually fitting an affine homography using the ubiquitous patch tracking method from [5]. The frequency-of-contact \mathbf{F} was then recovered using Eq. (4). The affine tracker was initialized by tracking a 100×100 pixel patch sub-sampled to 4000 pixels. However, note that the patch size in pixels changes dramatically during fixation as the tracked patch grows and shrinks in area as illustrated by Fig. 3.

Then, the τ -constraint was fused with the IMU measurements using a 2 second signal history and a 100 Hz sampling rate using linear interpolation. If the the average power of the bias corrected acceleration along an axis was below 2 m/s^2 the resulting depth from the τ -constraint was not used. If no observations of depth were available the depth estimate was forward propagated in time using the frequency of contact measurements (which are always available). The Luenberger's gain was set to $L = \text{diag}(2, 20)$ for all the sequences. Also, it is impor-

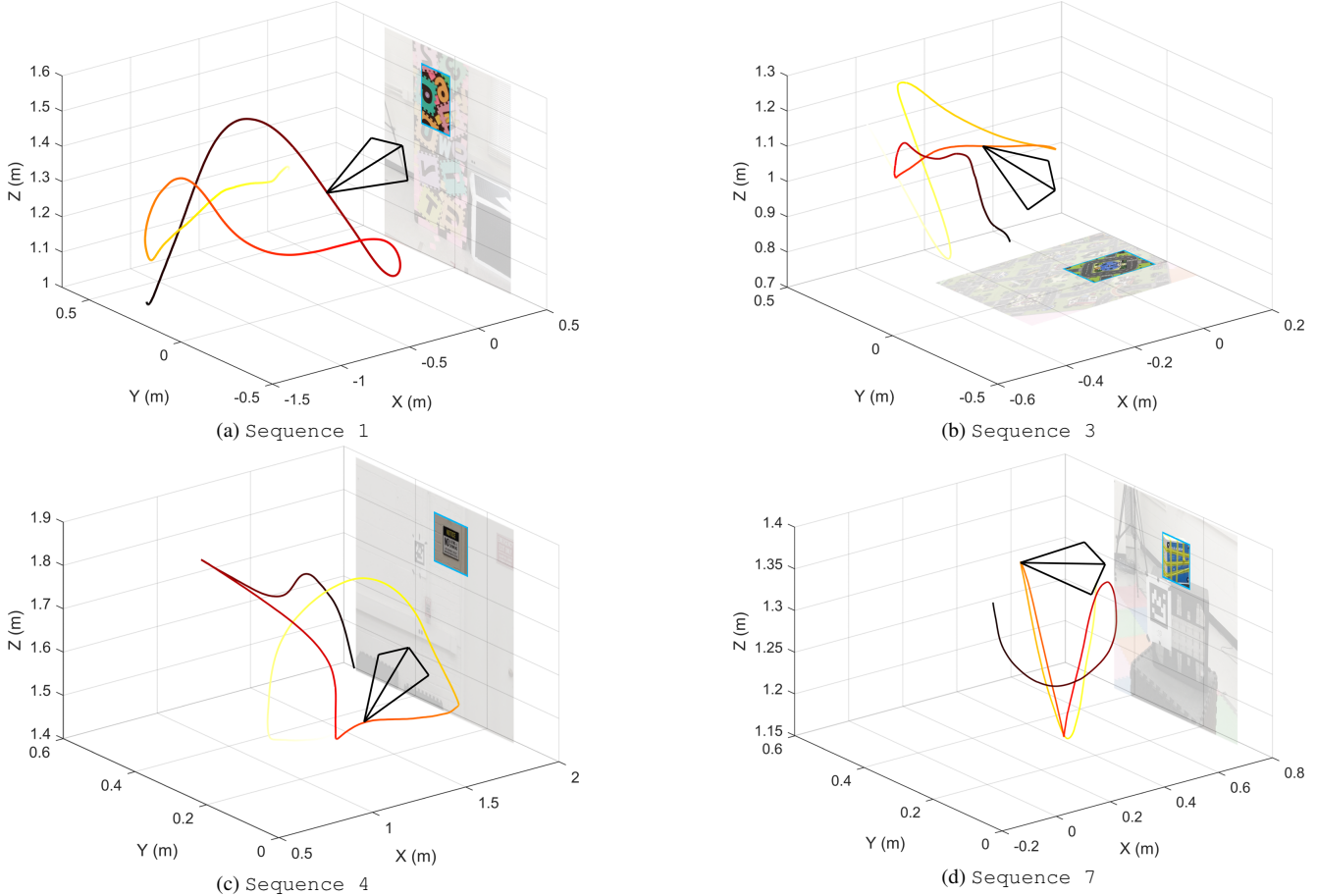


Figure 5. Five second sample camera trajectories for various sequences that are used to evaluate our novel τ -constraint that uses a monocular camera and an IMU to evaluate the depth of a scene patch. Fixation is illustrated by the highlighted scene region. Time is color coded with the hot colormap.

tant to note, that these parameters were not tuned using the sequences considered in this paper.

Our implementation is prototyped in Python 3.8 using standard scientific Python libraries with all processing done on a CPU. Numba is used to accelerate a few critical sections such as the affine tracker and the computation of integrals over time [21]. Two threads on a Intel[®] Core[™] i7-6820HQ laptop processor were used to perform all computations.

The open-source VINS-Mono and ROVIO implementations provided by their respective authors were used for comparison [7, 8, 27]. VINS-Mono was configured to output poses at 90 Hz (the camera frame-rate), however it produced poses only at 80 Hz. ROVIO was configured to produce poses at 90 Hz.

As another source of comparison we used the standard AprilTag 3 [20] library with the 36h11 tag family to detect AprilTags and their corner locations. The corners were used to solve the Perspective-n-Point problem to recover

the tag’s location in the current frame. The integrated gyroscope measurements were used to rotate each AprilTag pose measurement back to the fixed orientation used by the τ -constraint.

We also measured the ground truth trajectory using a Vicon motion capture system with 8 Vantage V8 cameras at 200 Hz.

We use the Trajectory Evaluation toolbox from [33] to align all trajectories to the Vicon ground truth. Average Trajectory Error (ATE) is calculated as described in [33] as

$$\text{ATE}(\mathbf{X}, \mathbf{X}^v) = \left(\frac{1}{N} \sum_{n=0}^{N-1} \|\mathbf{X}_n - \mathbf{X}_n^v\|_2^2 \right)^{1/2}. \quad (17)$$

Here \mathbf{X}^v is the Vicon’s trajectory estimate and \mathbf{X} is the trajectory under evaluation after alignment. N is the number of Vicon measurements in the considered time window. The trajectory under evaluation was linearly interpolated in order to evaluate the ATE.

Seq.	1	2	3	4	5	6	7	8	9	10
Sequence Duration (s)	14.99	26.14	32.22	36.23	16.35	16.27	8.02	32.15	26.75	40.07
Distance Traveled (m)	15.71	29.65	22.14	34.75	15.56	15.78	7.30	26.75	21.40	35.36
Method	ATE (cm) ↓									
AprilTag 3 [20]	2.88	-	2.66	-	3.77	-	0.66	-	2.55	-
VINS-Mono [27]	5.39	8.79	14.21	15.37	-	6.11	1.15	18.45	13.07	4.34
ROVIO [7, 8]	7.55	9.89	11.86	33.23	29.96	2.84	0.69	3.93	16.62	3.79
τ -constraint (ours)	8.06	6.91	11.96	10.27	16.80	7.21	10.70	4.34	2.38	3.24
τ -constraint (ours) (30 Hz LK output)	7.75	6.59	12.43	15.04	17.40	8.18	5.91	4.75	3.63	3.49
τ -constraint (ours) (15 Hz LK output)	9.81	7.59	16.17	19.29	14.96	8.70	5.86	5.37	3.47	3.48

Table 1. Sequence duration (second), path length (meters), and each method’s accuracy in centimeters of Average Trajectory Error (ATE).

Since the different trajectory estimation methods require different amounts of time to initialize, after which they produce position estimates, we perform the alignment and ATE calculation over the sequences’ time period where measurements were available from all sources. The duration and path length for each sequence were also calculated over this time period.

Because the accuracy of the numerical methods used to evaluate integrals is affected by the sampling rate, in additional experiments we reduced the output of the LK tracker from 90 Hz to 30 Hz and 15 Hz. The results illustrate the effect of low-framerate input on the τ -constraint’s accuracy.

6. Results

The ATE results across all the 10 sequences are given in Tab. 1 along with the path length and duration of the sequence. The proposed τ -constraint achieves a lower ATE than VINS-Mono in six out of nine comparable sequences and a lower ATE than ROVIO in 5 out of 10 comparable sequences. ATE averaged over all sequences was 8.5 cm for our method, 16.9 cm for ROVIO, and 2.8 cm for AprilTag 3. The average ATE for VINS-Mono, averaged over all sequences except sequence 5 was 12.2 cm. The VINS-Mono result is omitted for sequence 5 because its trajectory estimate diverged.

It is no surprise that the AprilTag method for pose estimation routinely achieved the best ATE. This is because the AprilTag system uses the known size of the visual fiducial to estimate depth. Regardless, the τ -constraint performs comparably to the AprilTag method in some sequences. This is particularly noticeable in Sequence 9. In Fig. 1 the instantaneous l_2 error of each method in Sequence 9 is plotted for comparison.

Lowering the sample rate going from the LK-tracker to the τ -constraint from 90 to 30 and 15 Hz had a relatively small effect on accuracy. In a few sequences, the ATE error actually decreased. This is probably because the bandwidth

of the cameras trajectory is limited to a few hertz since the camera was moved by hand and because decimation can have a similar effect as low-pass filtering.

While the ATE errors are promising, they do not indicate that our method is better than existing VIO methods. Such a claim would require the development of a full VIO stack around the τ -constraint and comparisons on existing VIO datasets. Developing a full VIO stack around the τ -constraint is far beyond the scope of this paper. Regardless, the ATE errors are very promising and indicate that development of the τ -constraint is a promising direction for future work to enhance the capabilities of current VIO and SLAM. We believe this would help achieve a new state-of-the-art.

The speed of our method was much higher than VINS-Mono and ROVIO. Our Python implementation achieved an average performance of $7.14 \times$ realtime or 642 frames per second (fps). VINS-Mono’s C++ implementation ran at $0.26 \times$ realtime or 23.6 fps. ROVIO’s C++ implementation ran at $1.05 \times$ realtime or 94.5 fps.

7. Limitations and Future Work

The main limitation of the τ -constraint is that there must be acceleration for the constraint to be useful. However, this is a fundamental constraint of all monocular geometric methods that are not coupled with a position or velocity sensor. A related limitation is that our method of using least-squares with the τ -constraint introduces the additional condition that jerk (change of acceleration) must be non-zero at some point during the measurement window. In practice we found sinusoidal accelerations with approximately 2 m/s^2 of power were necessary to get good measurements. Future work should investigate this carefully from a thorough mathematical and empirical perspective. Additionally, it may be of interest to the robotics community to investigate actively controlling the agent in order to use the τ -constraint.

For our method to be deployable in-the-wild, one would

need to fixate (track) on multiple patches and actively switch between them as necessary to obtain robust pose for fast movement when one or more patches enter and leave the field of view. Such a method would result in a fully functional VIO system built upon the τ -constraint. Based on our preliminary results, we believe this to be a promising avenue for future research.

8. Conclusion

A new mathematical constraint between time-to-contact (τ), acceleration, and depth, called the τ -constraint, was presented. To validate the practical efficacy of the constraint, a series of experiments in a trajectory estimation task were conducted using inexpensive and commercially available sensors. The results were particularly promising. Our method ran $6.8\times$ to $27\times$ faster than two state-of-the-art VIO methods that would typically be used for the same task, while achieving 30% to 50% less absolute trajectory error. This speedup is largely due to using only a small portion (initially 2.5%) of the image. These results indicate that further development of the τ -constraint, in theory and practice, is a promising direction for VIO, VI-SLAM, active perception, and robotics.

References

- [1] John Aloimonos, Isaac Weiss, and Amit Bandyopadhyay. Active vision. *International Journal of Computer Vision*, 1(4):333–356, 1988. [1](#)
- [2] Abhishek Badki, Orazio Gallo, Jan Kautz, and Pradeep Sen. Binary TTC: A temporal geofence for autonomous navigation. In *Proceedings of the IEEE/CVF Conference on Computer Vision and Pattern Recognition*, pages 12946–12955, 2021. [2](#)
- [3] Ruzena Bajcsy. Active perception. *Proceedings of the IEEE*, 76(8):966–1005, 1988. [1](#)
- [4] Ruzena Bajcsy, Yiannis Aloimonos, and John K. Tsotsos. Revisiting active perception. *Autonomous Robots*, 42:177–196, 2018. [2](#)
- [5] Simon Baker and Iain Matthews. Lucas-Kanade 20 years on: A unifying framework. *International Journal of Computer Vision*, 56(3):221–255, 2004. [6](#)
- [6] Dana H. Ballard. Animate vision. *Artificial Intelligence*, 48(1):57–86, 1991. [1](#), [2](#)
- [7] Michael Bloesch, Michael Burri, Sammy Omari, Marco Hutter, and Roland Siegwart. Iterated extended Kalman filter based visual-inertial odometry using direct photometric feedback. *The International Journal of Robotics Research*, 36(10):1053–1072, 2017. [7](#), [8](#)
- [8] Michael Bloesch, Sammy Omari, Marco Hutter, and Roland Siegwart. Robust visual inertial odometry using a direct EKF-based approach. In *2015 IEEE/RSJ International Conference on Intelligent Robots and Systems (IROS)*, pages 298–304, 2015. [3](#), [7](#), [8](#)
- [9] Ronald Clark, Sen Wang, Hongkai Wen, Andrew Markham, and Niki Trigoni. VINet: Visual-inertial odometry as a sequence-to-sequence learning problem. In *Proceedings of the Thirty-First AAAI Conference on Artificial Intelligence*, volume 31, pages 3995–4001, 2017. [3](#)
- [10] Guido C H E de Croon. Monocular distance estimation with optical flow maneuvers and efference copies: a stability-based strategy. *Bioinspiration & Biomimetics*, 11(1):016004, 2016. [2](#)
- [11] Cornelia Fermüller. Navigational preliminaries. In Yiannis Aloimonos, editor, *Active Perception*, chapter 3, pages 103–150. Lawrence Erlbaum Assoc., Hillsdale, NJ, 1993. [1](#)
- [12] Cornelia Fermüller and Yiannis Aloimonos. Tracking facilitates 3-D motion estimation. *Biological Cybernetics*, 67(3):259–268, 1992. [2](#)
- [13] Liming Han, Yimin Lin, Guoguang Du, and Shiguo Lian. DeepVIO: Self-supervised deep learning of monocular visual inertial odometry using 3D geometric constraints. In *2019 IEEE/RSJ International Conference on Intelligent Robots and Systems (IROS)*, pages 6906–6913. IEEE, 2019. [3](#)
- [14] João P. Hespanha. *Linear Systems Theory*. Princeton University Press, 2nd edition, 2018. [6](#)
- [15] Hann Woei Ho, Guido CHE de Croon, and Qiping Chu. Distance and velocity estimation using optical flow from a monocular camera. *International Journal of Micro Air Vehicles*, 9(3):198–208, 2017. [2](#)
- [16] Berthold K.P. Horn, Yajun Fang, and Ichiro Masaki. Time to contact relative to a planar surface. In *2007 IEEE Intelligent Vehicles Symposium*, pages 68–74, 2007. [2](#)
- [17] Vadim Indelman, Stephen Williams, Michael Kaess, and Frank Dellaert. Information fusion in navigation systems via factor graph based incremental smoothing. *Robotics and Autonomous Systems*, 61(8):721–738, 2013. [2](#)
- [18] Nitin Jagannatha Sanket. *Active Vision Based Embodied-AI Design for Nano-UAV Autonomy*. PhD thesis, University of Maryland, College Park, 2021. [1](#)
- [19] Leonid Keselman, John Iselin Woodfill, Anders Grunnet-Jepsen, and Achintya Bhowmik. Intel(R) RealSense(TM) stereoscopic depth cameras. In *2017 IEEE Conference on Computer Vision and Pattern Recognition Workshops (CVPRW)*, pages 1267–1276, 2017. [6](#)
- [20] Maximilian Krogus, Acshi Haggenmiller, and Edwin Olson. Flexible layouts for fiducial tags. In *2019 IEEE/RSJ International Conference on Intelligent Robots and Systems (IROS)*, pages 1898–1903, 2019. [2](#), [7](#), [8](#)
- [21] Siu Kwan Lam, Antoine Pitrou, and Stanley Seibert. Numba: A LLVM-based Python JIT compiler. In *Proceedings of the Second Workshop on the LLVM Compiler Infrastructure in HPC*, pages 7:1–7:6, 2015. [7](#)
- [22] David N. Lee. A theory of visual control of braking based on information about time-to-collision. *Perception*, 5(4):437–459, 1976. [2](#)
- [23] David N Lee, Reinoud J Bootsma, Mike Land, David Regan, and Rob Gray. Lee’s 1976 paper. *Perception*, 38(6):837–858, 2009. [2](#)
- [24] Agostino Martinelli. Vision and IMU data fusion: Closed-form solutions for attitude, speed, absolute scale, and bias determination. *IEEE Transactions on Robotics*, 28(1):44–60, 2012. [3](#)

- [25] Agostino Martinelli. Closed-form solution of visual-inertial structure from motion. *International Journal of Computer Vision*, 106(2):138–152, 2014. 3
- [26] Anastasios I. Mourikis and Stergios I. Roumeliotis. A multi-state constraint Kalman filter for vision-aided inertial navigation. In *Proceedings of the 2007 IEEE International Conference on Robotics and Automation*, pages 3565–3572, 2007. 3
- [27] Tong Qin, Peiliang Li, and Shaojie Shen. VINS-Mono: A robust and versatile monocular visual-inertial state estimator. *IEEE Transactions on Robotics*, 34(4):1004–1020, 2018. 2, 3, 7, 8
- [28] Nitin J Sanket, Chahat Deep Singh, Cornelia Fermüller, and Yiannis Aloimonos. PRGFlow: Unified SWAP-aware deep global optical flow for aerial robot navigation. *Electronics Letters*, 57(16):614–617, 2021. 3
- [29] Nitin J. Sanket, Chahat Deep Singh, Kanishka Ganguly, Cornelia Fermüller, and Yiannis Aloimonos. GapFlyt: Active vision based minimalist structure-less gap detection for quadrotor flight. *IEEE Robotics and Automation Letters*, 3(4):2799–2806, 2018. 2
- [30] Fendy Santoso, Matthew A. Garratt, and Sreenatha G. Anavatti. Visual-inertial navigation systems for aerial robotics: Sensor fusion and technology. *IEEE Transactions on Automation Science and Engineering*, 14(1):260–275, 2017. 2
- [31] Olaf Sikorski, Dario Izzo, and Gabriele Meoni. Event-based spacecraft landing using time-to-contact. In *Proceedings of the IEEE/CVF Conference on Computer Vision and Pattern Recognition (CVPR) Workshops*, pages 1941–1950, 2021. 2
- [32] Celyn Walters and Simon Hadfield. EVReflex: Dense time-to-impact prediction for event-based obstacle avoidance. In *2021 IEEE/RSJ International Conference on Intelligent Robots and Systems (IROS)*, pages 1304–1309, 2021. 2
- [33] Zichao Zhang and Davide Scaramuzza. A tutorial on quantitative trajectory evaluation for visual(-inertial) odometry. In *2018 IEEE/RSJ International Conference on Intelligent Robots and Systems (IROS)*, pages 7244–7251, 2018. 7

Supplementary Material - Fast Active Monocular Distance Estimation from Time-to-Contact

1. Affine Homography to Affine Flow

The manuscript begins with the definition of an affine flow field, however the affine flow parameters were obtained through a finite-difference approximation of the derivative of the parameters of an affine homography. Below, for clarity, we show how this can be done.

Suppose P denotes the initial set of points of in an image patch that correspond with a planar object. The affine homography \mathcal{W} assumes the following brightness constancy constraint.

$$I(t, \mathcal{W}(t, \mathbf{x}(t))) = I(0, \mathbf{x}(0)), \quad \forall \mathbf{x}(0) \in P$$

$$\mathcal{W}(t, \mathbf{x}) = \mathbf{x}(t) := \underbrace{\begin{bmatrix} w_1 & w_2 & w_3 \\ w_4 & w_5 & w_6 \\ 0 & 0 & 1 \end{bmatrix}}_{W(t)}(t)\mathbf{x}(0) \quad (18)$$

Where I is the image intensity function and W is the matrix transformation that defines the warp function \mathcal{W} . The implementation uses the following finite-difference approximation to estimate the affine flow parameters ($A(t)$).

$$\begin{aligned} \mathbf{u}(t)T &\approx \mathbf{x}(t) - \mathbf{x}(t-T) \\ &= (W(t) - W(t-T))\mathbf{x}(0) \\ &= \underbrace{(W(t) - W(t-T))W^{-1}(t)}_{\approx A(t)T}\mathbf{x}(t) \end{aligned} \quad (19)$$

Where $T > 0$. It is easy to show that W^{-1} is an affine transformation and so $(W(t) - W(t-T))W^{-1}(t)$ is also an affine transformation. It is important to note the W^{-1} exists so long as all the points on a patch have not moved to a line or a point, that is $W^{-1}(t)$ exists as long as the patch is still a patch in the field of view.

2. Completion of Proof of Theorem 3.1

For brevity, the manuscript left out the complete proof of Theorem 3.1. Here we present the last remaining step which is to show the differential equation defined by the frequency-of-contact \mathbf{F}

$$\dot{\mathbf{X}}(t) = \mathbf{F}(t)Z(t) \quad (20)$$

is solved by $\mathbf{X}(t)$.

$$\mathbf{X}(t) = \mathbf{X}(0) + \underbrace{t\mathbf{F}(0)Z(0)}_{\dot{\mathbf{X}}(0)} + \underbrace{\int_0^t \left(\int_0^\lambda \ddot{\mathbf{X}}(\lambda_2)d\lambda_2 \right) d\lambda}_{\Delta\{\ddot{\mathbf{X}}\}(t)} \quad (21)$$

We proceed directly. First suppose that at $t = 0$ the initial condition is $\mathbf{X}(0)$. Substituting $t = 0$ into Eq. (21) immediately reveals that the initial condition is satisfied. Next consider the derivative of $\mathbf{X}(t)$ as defined by Eq. (21)

$$\begin{aligned} \frac{d}{dt}\mathbf{X}(t) &= \dot{\mathbf{X}}(t) = \dot{\mathbf{X}}(0) + \int_0^t \ddot{\mathbf{X}}(\lambda_2)d\lambda_2 \\ &= \dot{\mathbf{X}}(0) + \dot{\mathbf{X}}(t) - \dot{\mathbf{X}}(0) \\ &= \mathbf{F}(t)Z(t) \end{aligned} \quad (22)$$

Therefore, the solution for position in terms of unknown initial position, unknown initial frequency-of-contact, and acceleration given by Eq. (21) satisfies the differential equation defined by frequency-of-contact Eq. (20). Thus, their solutions are equal given equal initial conditions.

3. Necessary and Sufficient Conditions for Z^* and g^* to be well-defined

Recall that the least squares problem for distance and gravitational acceleration was written as

$$\begin{aligned} Q &:= \begin{bmatrix} \|E_Z\|_2^2 & \langle E_Z, \Delta\{\mathbf{1}_{[0,T]}\} \rangle_2 \\ \langle E_Z, \Delta\{\mathbf{1}_{[0,T]}\} \rangle_2 & \|\Delta\{\mathbf{1}_{[0,T]}\}\|_2^2 \end{bmatrix} \\ c &:= 2 \left[\langle E_Z, \Delta\{a_Z^m\} \rangle_2 \quad \langle \Delta\{\mathbf{1}_{[0,T]}\}, \Delta\{a_Z^m\} \rangle_2 \right]^T \\ y &:= [Z(0) \quad g_Z]^T \end{aligned} \quad (23)$$

Where the measured signals E_Z and $\Delta(a_Z^m)$ are known in a closed window $([0, T], T \neq 0)$ of time and taken to be

zero outside. Similarly, $\mathbf{1}_{[0,T]}$ is the indicator function over the time window $[0, T]$.

Here we derive the necessary and sufficient condition for $Q > 0$, which implies the problem is well-posed. The proof that follows is for motion along the Z axis, however the proof for the X and Y axis motion proceed identically. Begin by replacing the Z subscript with X and Y and follow the same steps.

Additionally, in what follows we assume the trajectory, \mathbf{X} , is smooth so that all the needed derivatives exist and derivatives with respect to time of equal quantities are equal everywhere. We also assume $Z(0) \geq \epsilon > 0$ as in the manuscript.

Consider $Q = 0$ if and only if $|Q| = 0$, that is

$$|Q| = \|E_Z\|_2^2 \|\Delta\{\mathbf{1}_{[0,T]}\}\|_2^2 - (\langle E_Z, \Delta\{\mathbf{1}_{[0,T]}\} \rangle_2)^2 = 0 \quad (24)$$

Rearranging and taking the square roots of both sides reveals this is the Cauchy–Schwarz inequality, in the equality case.

$$\|E_Z\|_2 \|\Delta\{\mathbf{1}_{[0,T]}\}\|_2 = \langle E_Z, \Delta\{\mathbf{1}_{[0,T]}\} \rangle_2 \quad (25)$$

Thus, by Cauchy–Schwarz, the above is true if and only if $\exists \alpha \in \mathbb{R}$ such that

$$E_Z(t) = \alpha \Delta\{\mathbf{1}_{[0,T]}\}(t), \quad \forall t \in [0, T] \quad (26)$$

Recalling the definition of E_Z and $\Delta(t, 1)$, we mean

$$\begin{aligned} \alpha \frac{1}{2} t^2 &= \Phi_{F_Z}(t) - 1 - t F_Z(0) \\ \iff \alpha \frac{1}{2} t^2 &= \frac{Z(t)}{Z(0)} - \left(\frac{Z(0)}{Z(0)} + t \frac{\dot{X}_Z(0)}{Z(0)} \right) \\ \iff (Z(0)\alpha) \frac{1}{2} t^2 &= Z(t) - \left(Z(0) + t \dot{X}_Z(0) \right) \end{aligned} \quad (27)$$

The right hand side is equal to the double integral of the acceleration as can be seen by comparing to Eq. (21).

$$\iff (Z(0)\alpha) \frac{1}{2} t^2 = \int_0^t \left(\int_0^\lambda \ddot{X}_Z(\lambda_2) d\lambda_2 \right) d\lambda \quad (28)$$

Taking the derivative with respect to t twice reveals

$$Q = 0 \iff \frac{Z(0)\alpha}{2} = \ddot{X}_Z(t), \quad \forall t \in [0, T] \quad (29)$$

Or, more simply,

$$Q = 0 \iff \frac{d}{dt} \ddot{X}_Z(t) = 0, \quad \forall t \in [0, T] \quad (30)$$

Recall, by definition $Q \succeq 0$. Therefore we have,

$$Q \succ 0 \iff \exists t \in [0, T] \quad \frac{d}{dt} \ddot{X}_Z(t) \neq 0 \quad (31)$$

Thus, the problem is well-posed if and only if there is non-zero jerk at some point during the window of signal history considered in the optimization problem.

4. Qualitative Properties of Sequences

The experiments were run on ten sequences from five scenes. Each scene is associated with two sequences, one with an AprilTag and one without. Recording without an AprilTag allowed more variation in the orientation of the camera because only one target needed to be kept in the field-of-view.

In Tab. 2 the defining qualitative features of each sequence are assessed and the defining metric quantities that cannot be easily seen from the trajectory plots are listed.

5. Sample Images, Trajectory, and Error Plots for all Sequences

Below, for each of the ten sequences, we show four sample images, X , Y , Z trajectory estimates, and l_2 error with regard to the Vicon ground truth for every trajectory estimation method available. The plots are to give a sense of the qualitative properties of each algorithm. All trajectories are aligned to the vicon ground-truth by a constant rotation and translation.

When run on Sequence 5, VINS-Mono diverged, so its results are not plotted for that sequence.

The biggest qualitative flaw with the τ -constraint’s estimates are occasional “spikes”. These are caused by occasional, large errors in the frequency-of-contact measurements that can happen as a result of the finite-difference scheme used. Future work could try to filter out the spikes or find a more elegant approach to calculating the integral of frequency of contact from the affine homography. However, because of the globally exponentially stable nature of the estimation and filtering methods used with the τ -constraint, its trajectory estimate always quickly converges back to the vicon ground-truth.

Seq.	Scene	Qualitative Properties				Metric Properties	
		Initial Orientation	Texture	Contrast	Orientation Variation	Duration (s)	Distance (m)
1	1	Parallel	Moderate	Moderate	Moderate	14.99	15.71
2	1	Parallel	Moderate	Moderate	High	26.14	29.65
3	2	Slanted	Moderate	High	Moderate	32.22	22.14
4	2	Slanted	Moderate	Moderate	High	36.23	34.75
5	3	Parallel	Low	Moderate	Low	16.35	15.56
6	3	Parallel	Low	Moderate	Moderate	16.27	15.78
7	4	Slanted	Moderate	Low	Moderate	8.02	7.30
8	4	Slanted	Moderate	Low	High	32.15	26.75
9	5	Parallel	High (repeated)	High	Moderate	26.75	21.40
10	5	Parallel	High (repeated)	High	High	40.07	35.36

Table 2. Qualitative assessment of the defining properties of the ten sequences. “Initial Orientation” is with regard to the initial imaging plane. “Texture” refers to the density of intensity gradients of varying direction. “Contrast” refers to the distribution of dark and bright pixels within the patch. “Orientation Variation” refers to the amount of orientation change throughout the sequence.

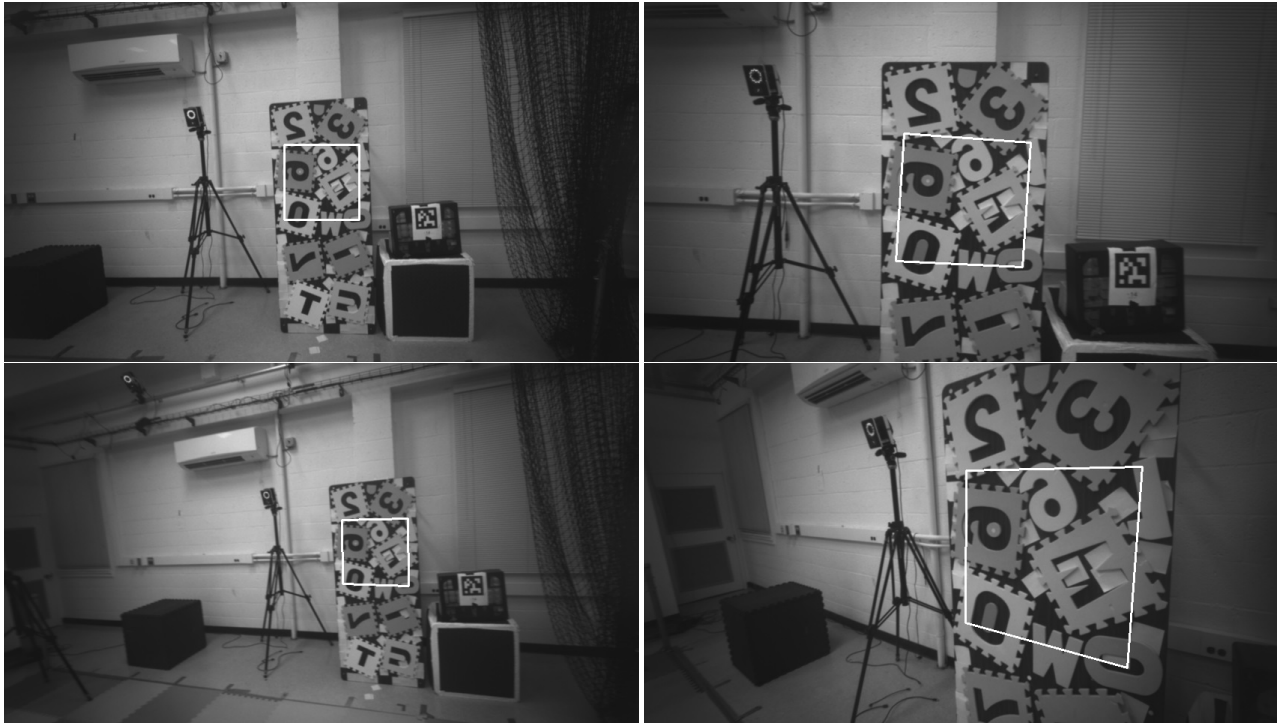


Figure 6. Four representative frames from Sequence 1. The tracked patch is indicated by the white box.

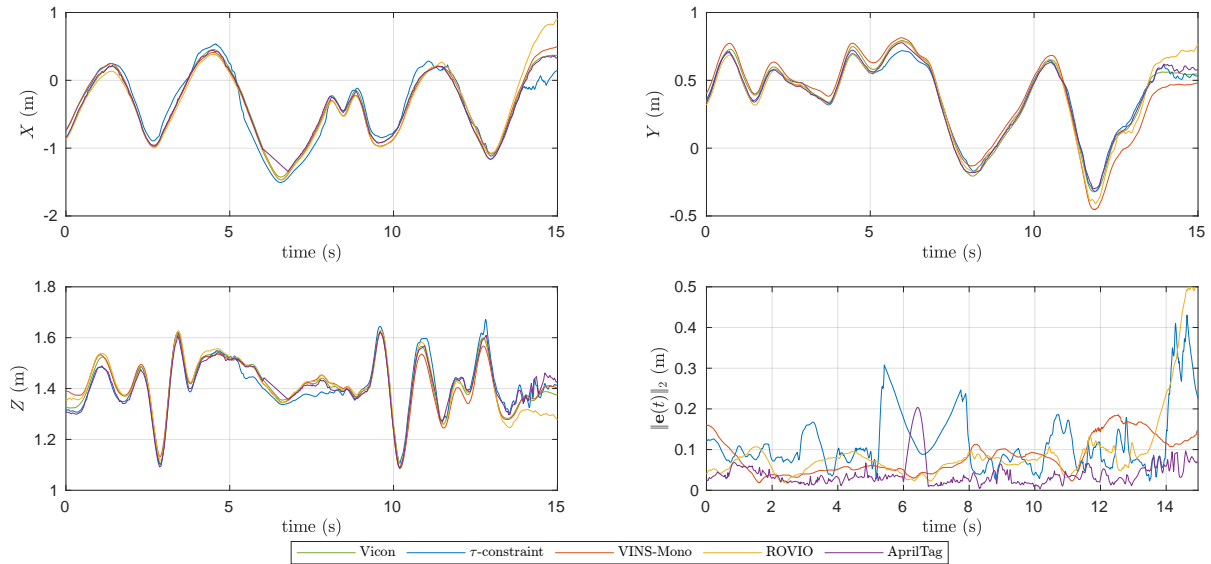


Figure 7. Sequence 1 estimated trajectories versus Vicon ground truth for all available estimation methods. All trajectories are aligned to the vicon by a rigid body transformation. (top-left) X axis trajectory, (top-right) Y axis trajectory, (bottom-left) Z axis trajectory, (bottom-right) l_2 error between estimated trajectories and Vicon ground truth.

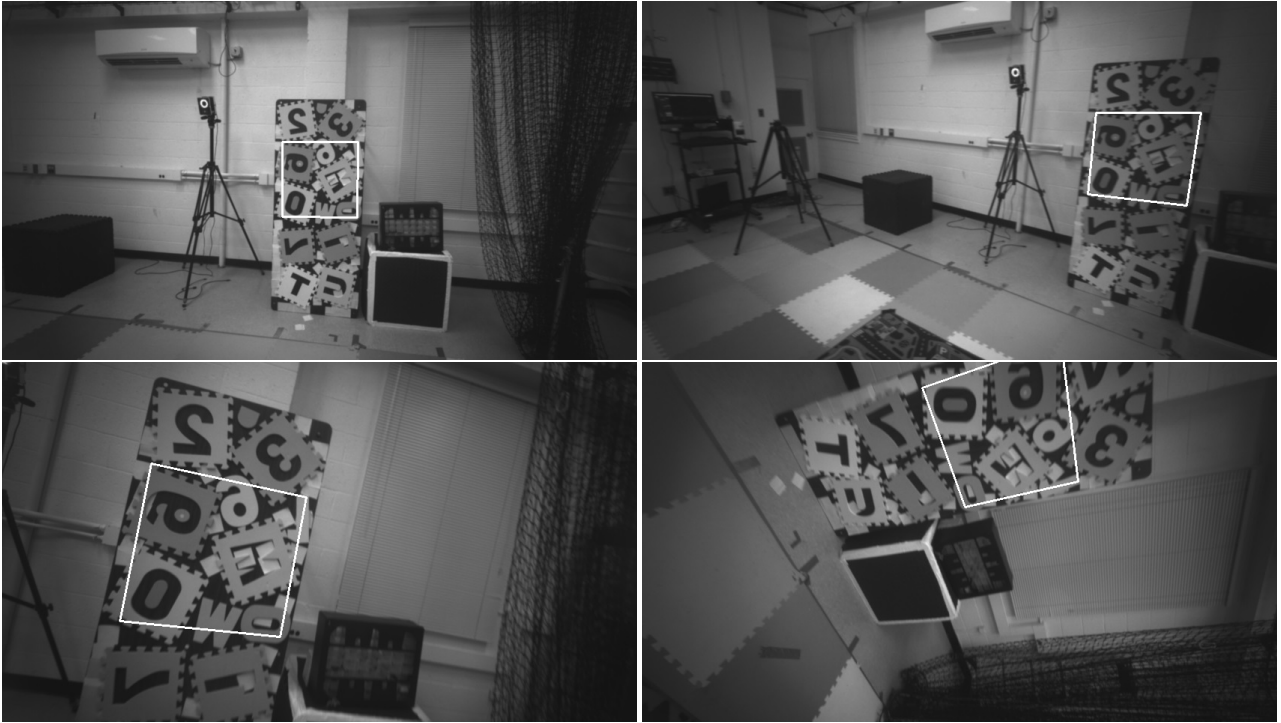


Figure 8. Four representative frames from Sequence 2. The tracked patch is indicated by the white box. This sequence does not contain an AprilTag.

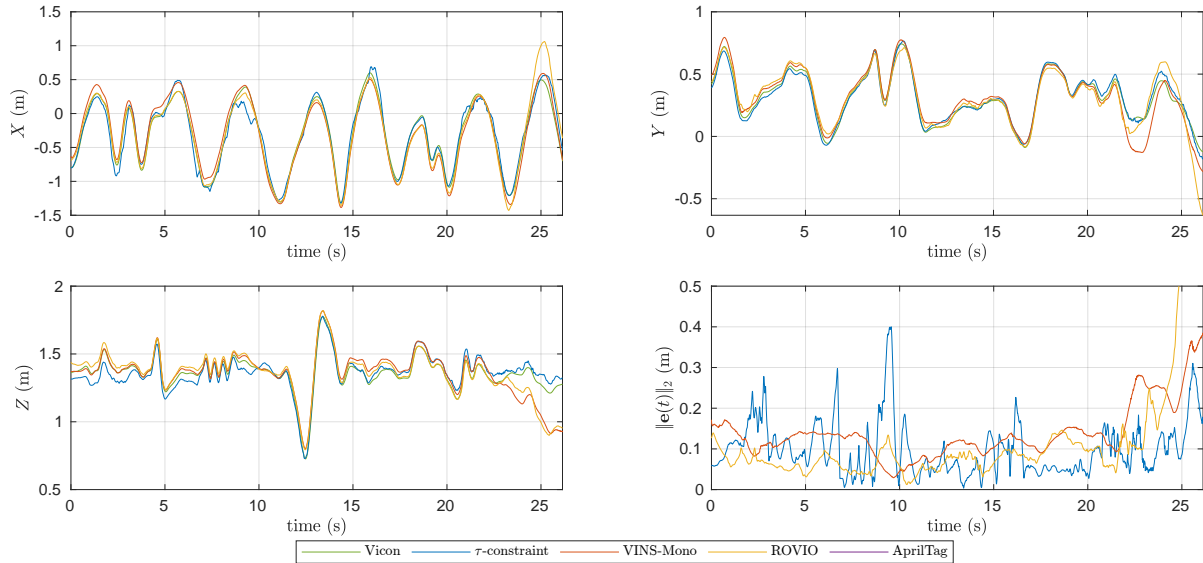


Figure 9. Sequence 2 estimated trajectories versus Vicon ground truth for all available estimation methods. All trajectories are aligned to the vicon by a rigid body transformation. (top-left) X axis trajectory, (top-right) Y axis trajectory, (bottom-left) Z axis trajectory, (bottom-right) l_2 error between estimated trajectories and Vicon ground truth.

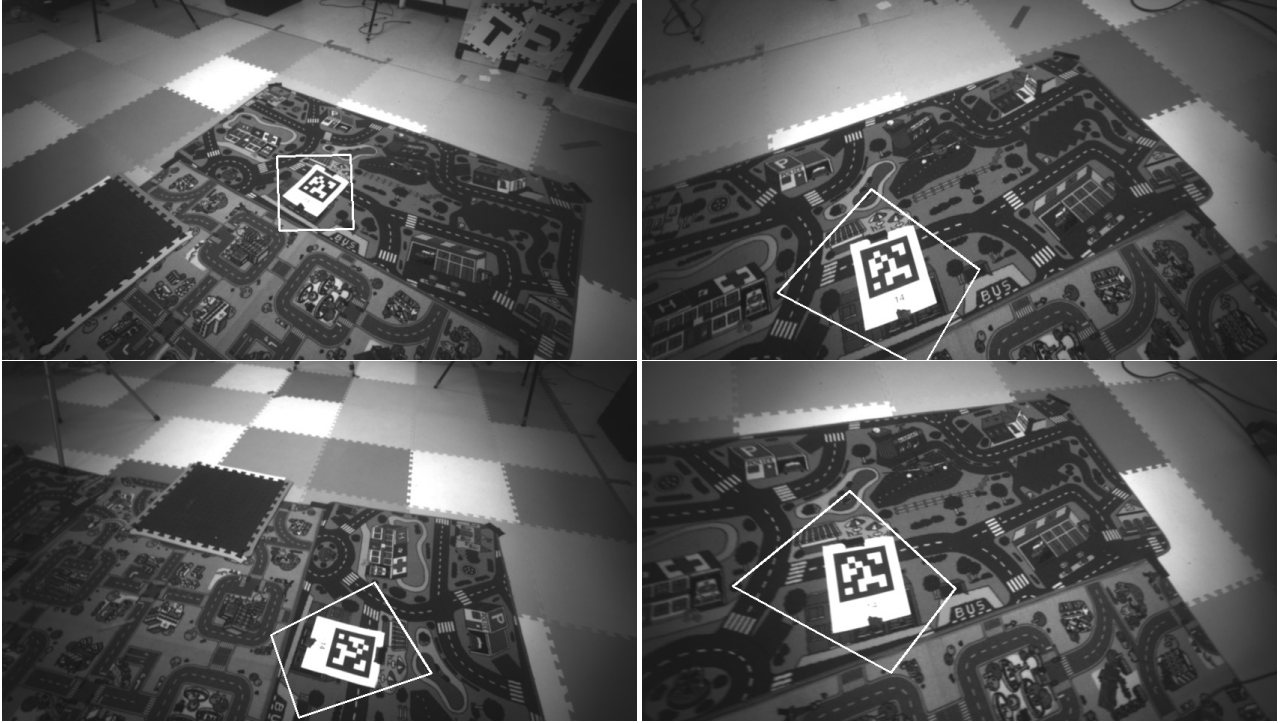


Figure 10. Four representative frames from Sequence 3. The tracked patch is indicated by the white box.

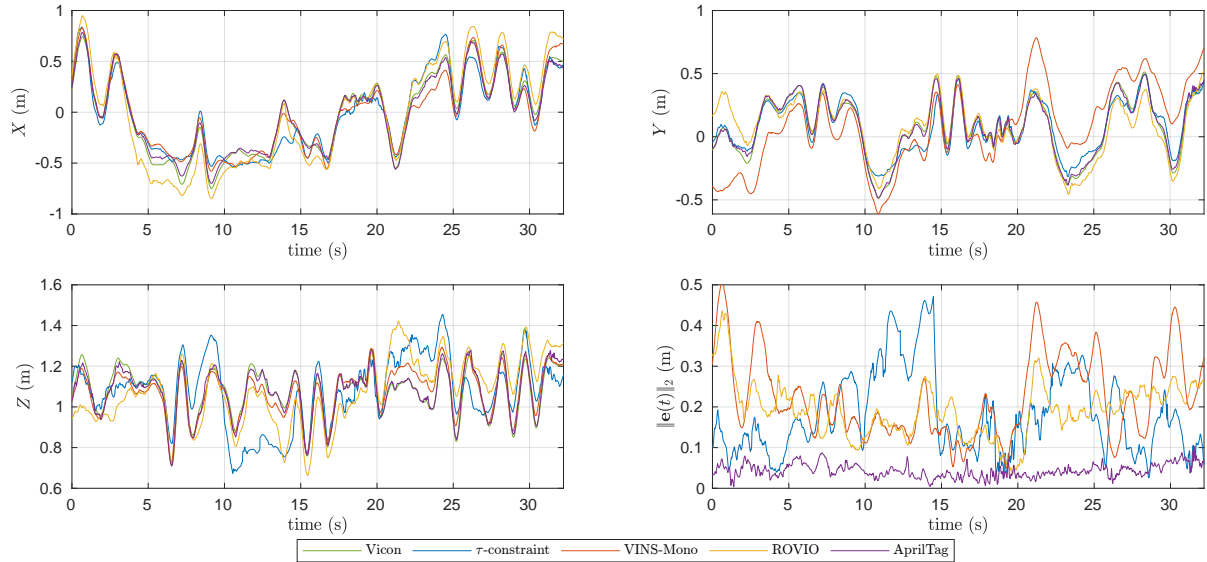


Figure 11. Sequence 3 estimated trajectories versus Vicon ground truth for all available estimation methods. All trajectories are aligned to the vicon by a rigid body transformation. (top-left) X axis trajectory, (top-right) Y axis trajectory, (bottom-left) Z axis trajectory, (bottom-right) l_2 error between estimated trajectories and Vicon ground truth.

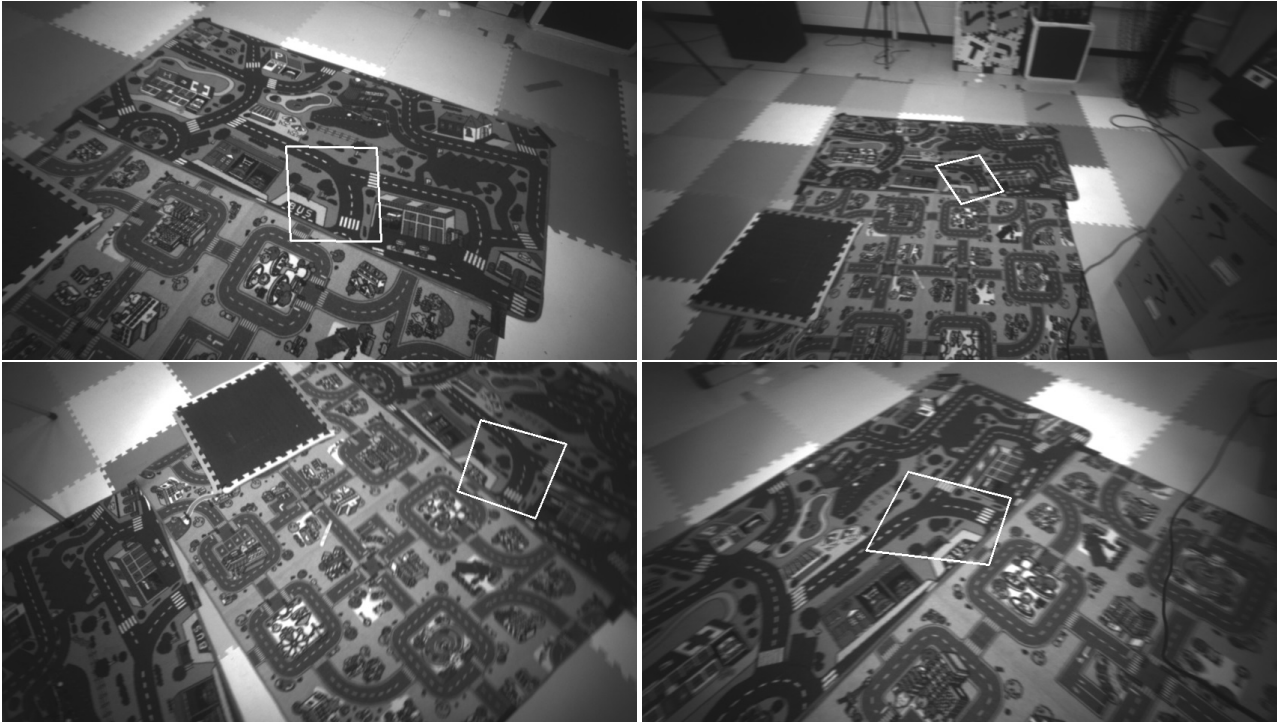


Figure 12. Four representative frames from Sequence 4. The tracked patch is indicated by the white box. This sequence does not contain an AprilTag.

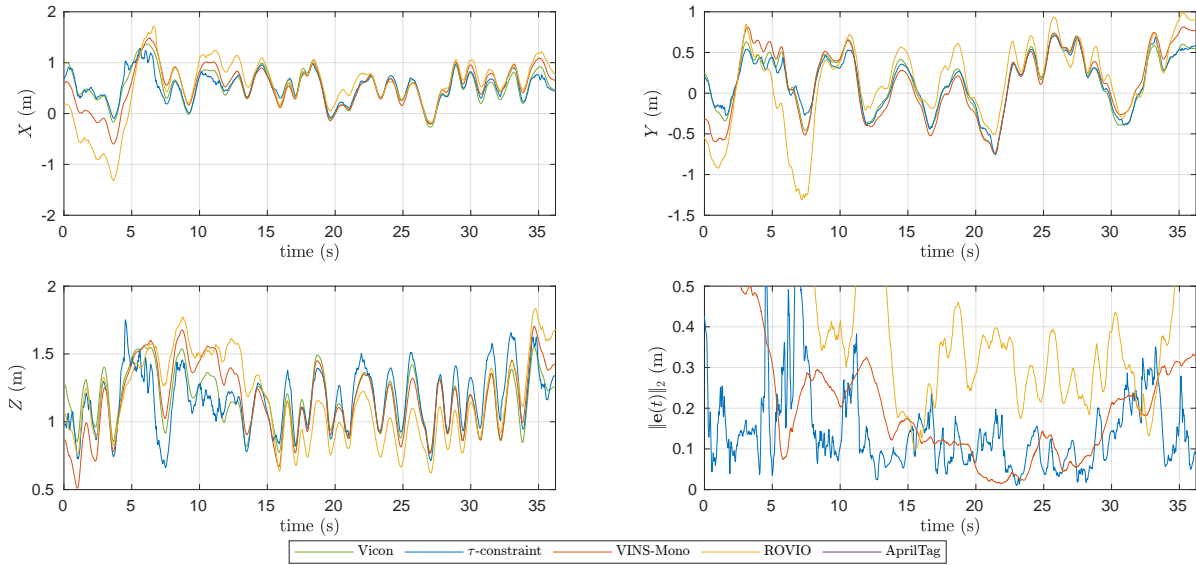


Figure 13. Sequence 4 estimated trajectories versus Vicon ground truth for all available estimation methods. All trajectories are aligned to the vicon by a rigid body transformation. (top-left) X axis trajectory, (top-right) Y axis trajectory, (bottom-left) Z axis trajectory, (bottom-right) l_2 error between estimated trajectories and Vicon ground truth.



Figure 14. Four representative frames from Sequence 5. The tracked patch is indicated by the white box.

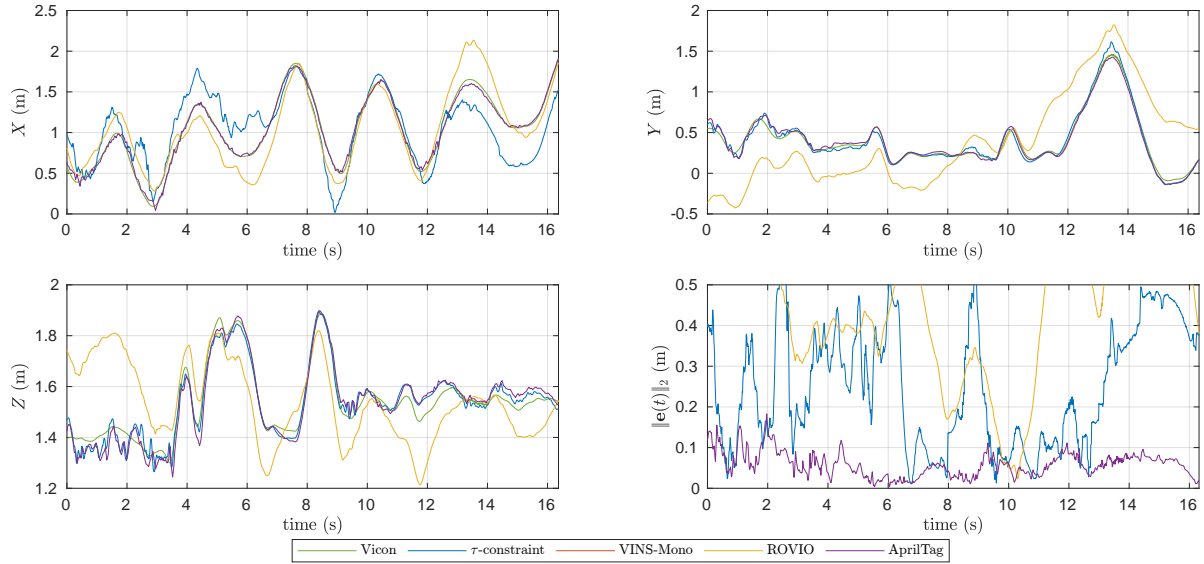


Figure 15. Sequence 5 estimated trajectories versus Vicon ground truth for all available estimation methods. VINS-Mono is left out because it diverged. All trajectories are aligned to the vicon by a rigid body transformation. (top-left) X axis trajectory, (top-right) Y axis trajectory, (bottom-left) Z axis trajectory, (bottom-right) l_2 error between estimated trajectories and Vicon ground truth.

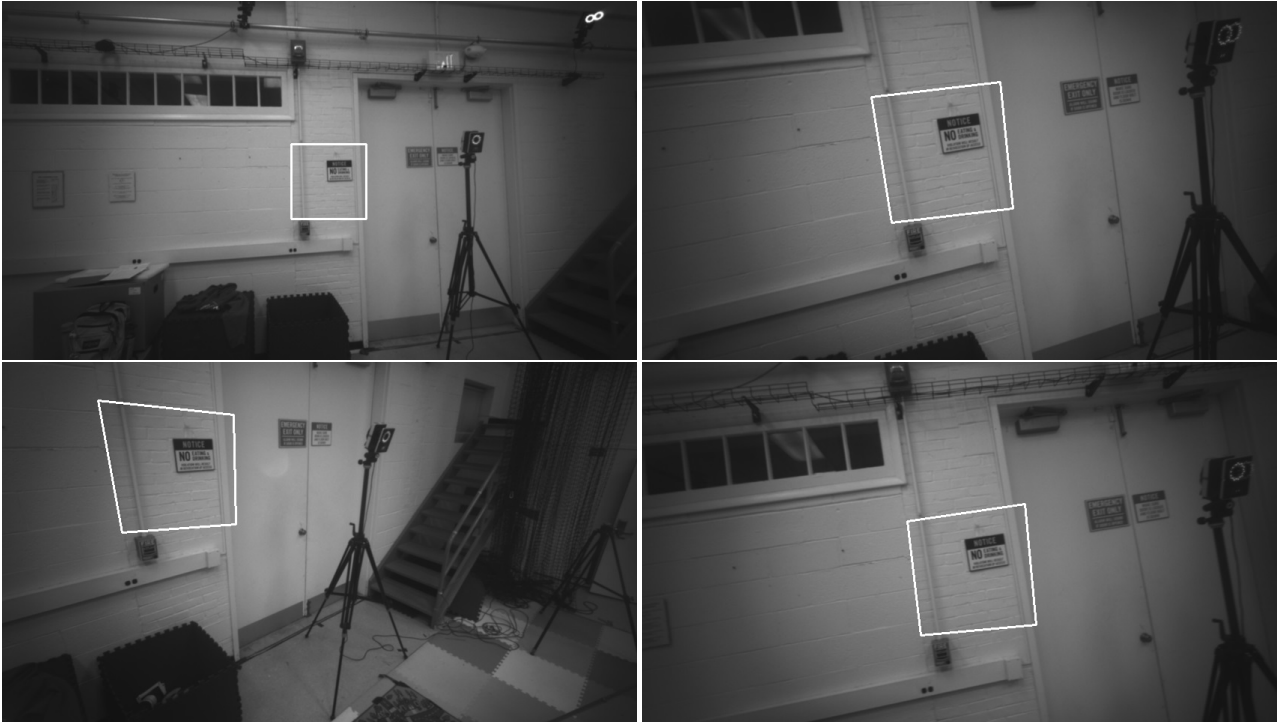


Figure 16. Four representative frames from Sequence 6. The tracked patch is indicated by the white box. This sequence does not contain an AprilTag.

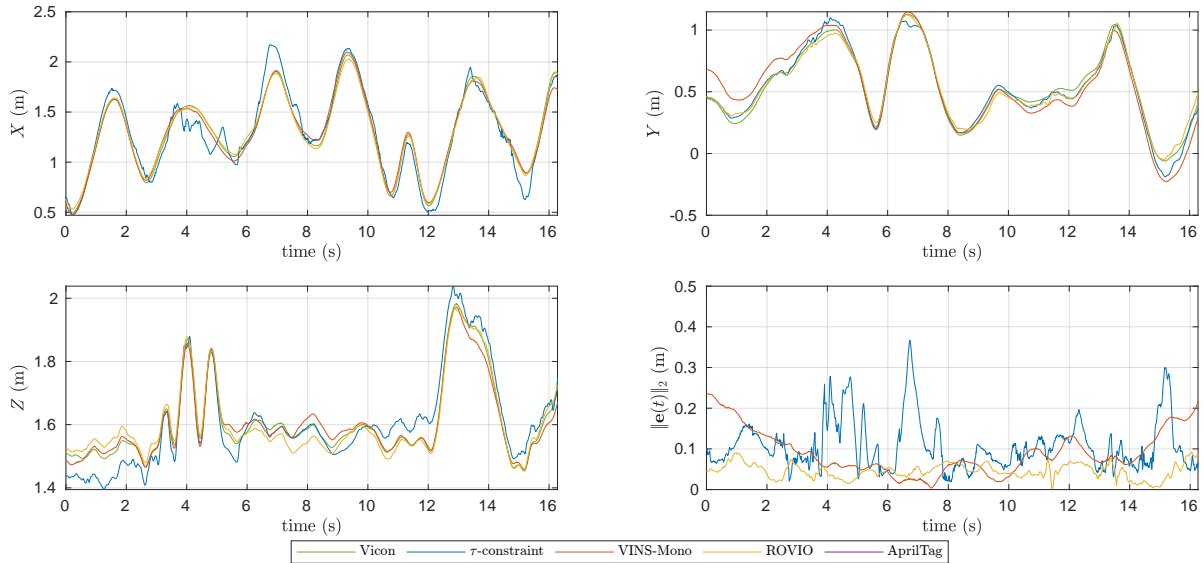


Figure 17. Sequence 6 estimated trajectories versus Vicon ground truth for all available estimation methods. All trajectories are aligned to the vicon by a rigid body transformation. (top-left) X axis trajectory, (top-right) Y axis trajectory, (bottom-left) Z axis trajectory, (bottom-right) l_2 error between estimated trajectories and Vicon ground truth.

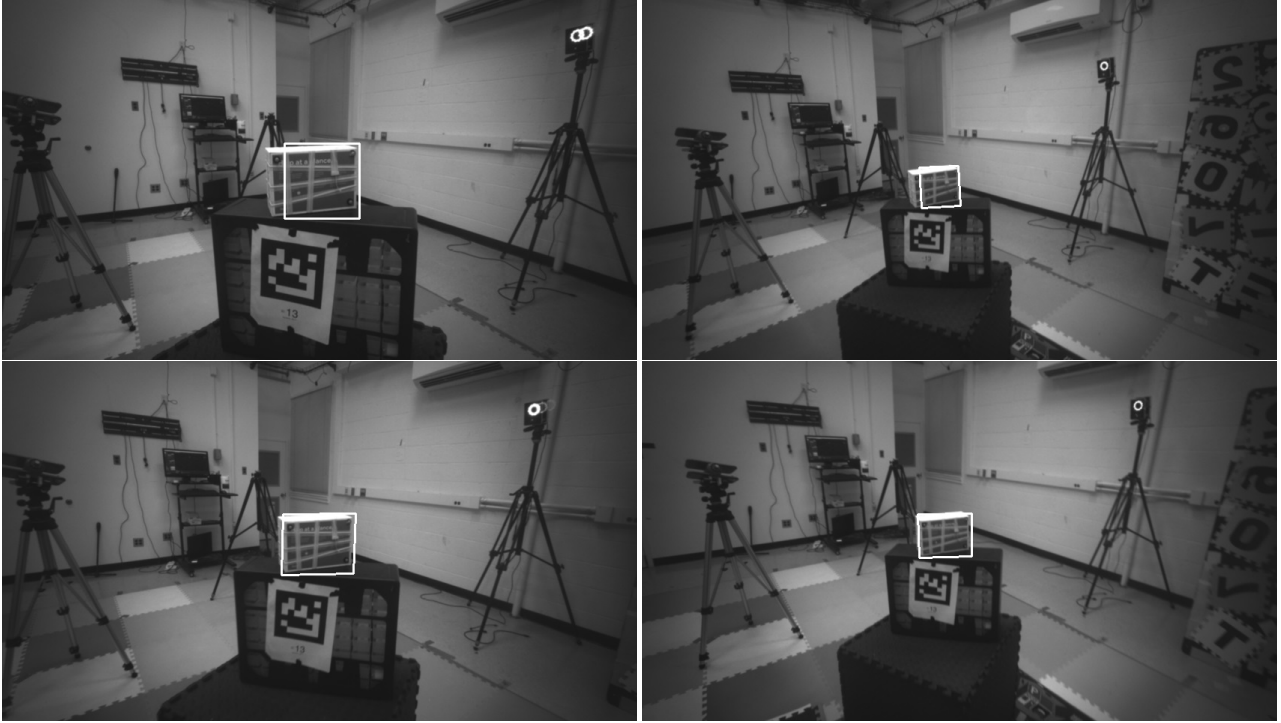


Figure 18. Four representative frames from Sequence 7. The tracked patch is indicated by the white box.

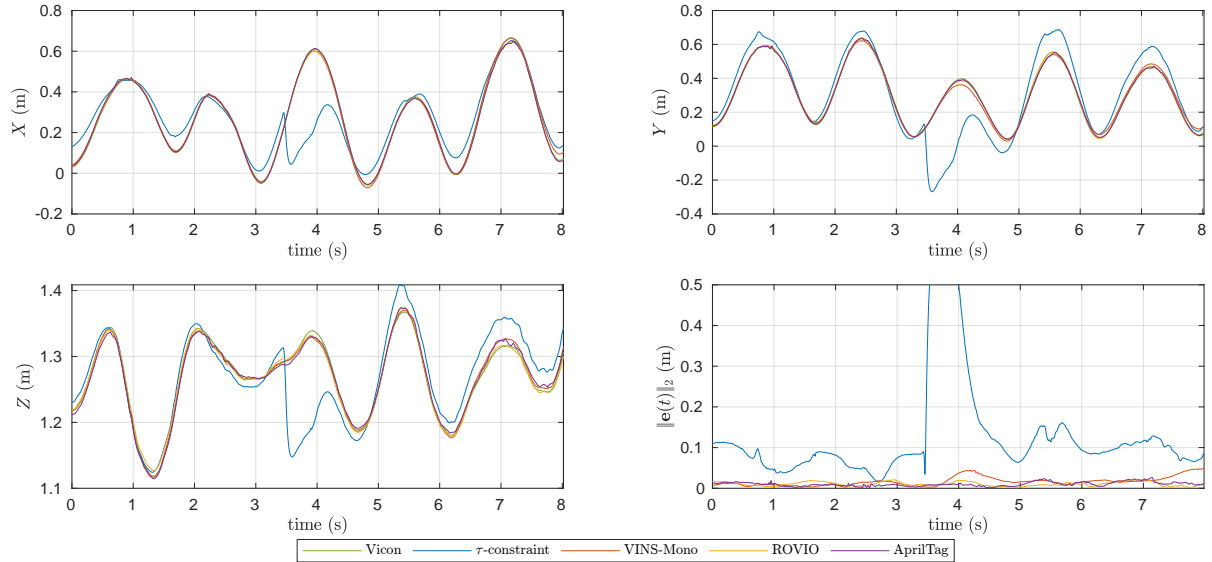


Figure 19. Sequence 7 estimated trajectories versus Vicon ground truth for all available estimation methods. All trajectories are aligned to the vicon by a rigid body transformation. (top-left) X axis trajectory, (top-right) Y axis trajectory, (bottom-left) Z axis trajectory, (bottom-right) l_2 error between estimated trajectories and Vicon ground truth.

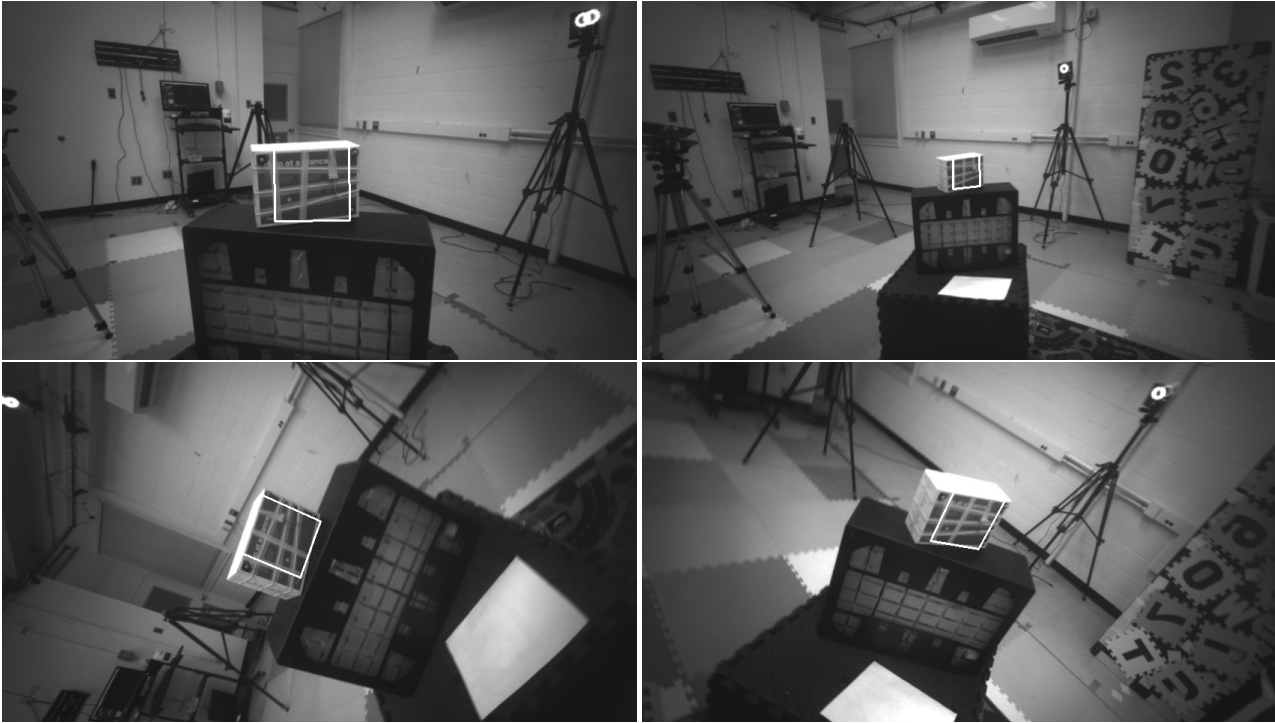


Figure 20. Four representative frames from Sequence 8. The tracked patch is indicated by the white box. This sequence does not contain an AprilTag.

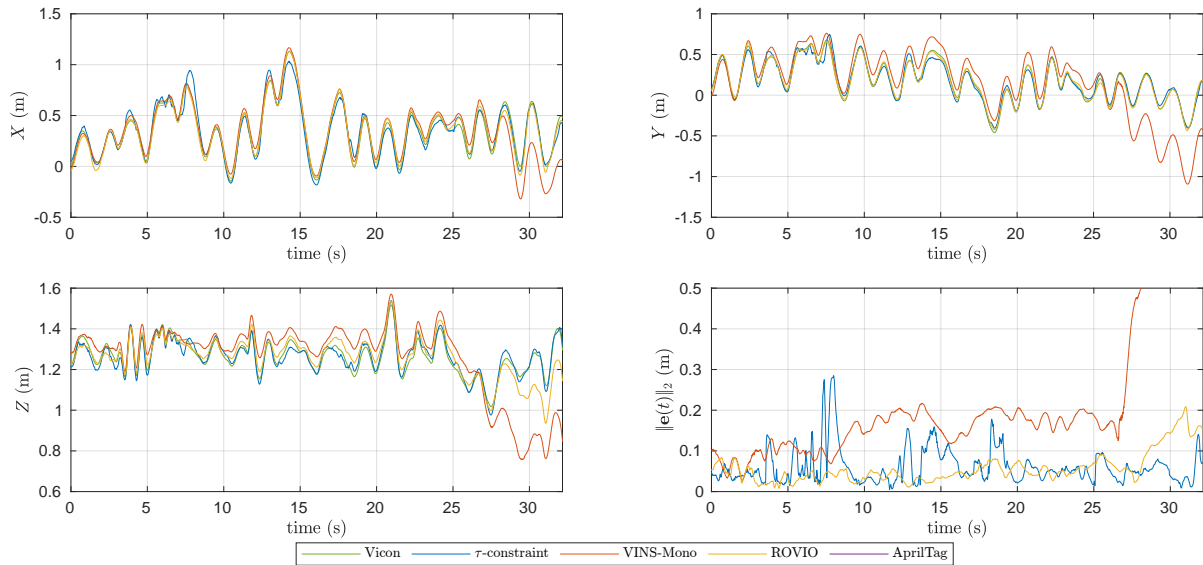


Figure 21. Sequence 8 estimated trajectories versus Vicon ground truth for all available estimation methods. All trajectories are aligned to the vicon by a rigid body transformation. (top-left) X axis trajectory, (top-right) Y axis trajectory, (bottom-left) Z axis trajectory, (bottom-right) l_2 error between estimated trajectories and Vicon ground truth.

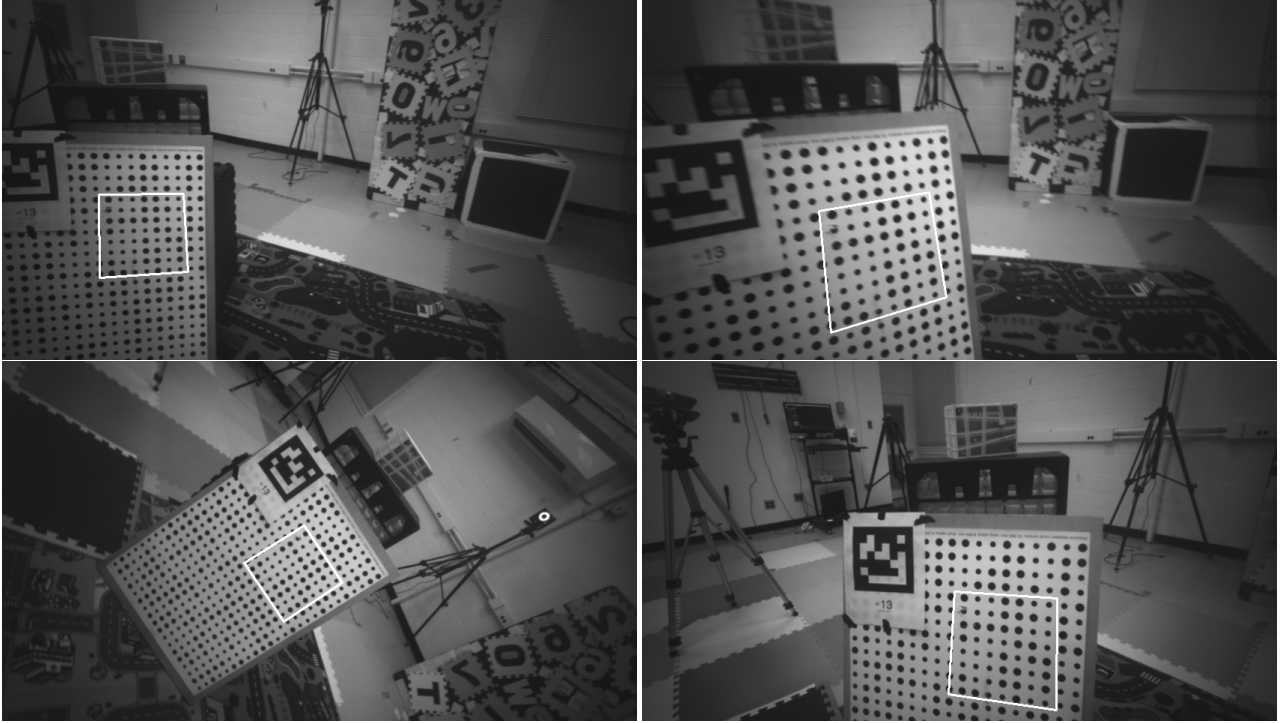


Figure 22. Four representative frames from Sequence 9. The tracked patch is indicated by the white box.

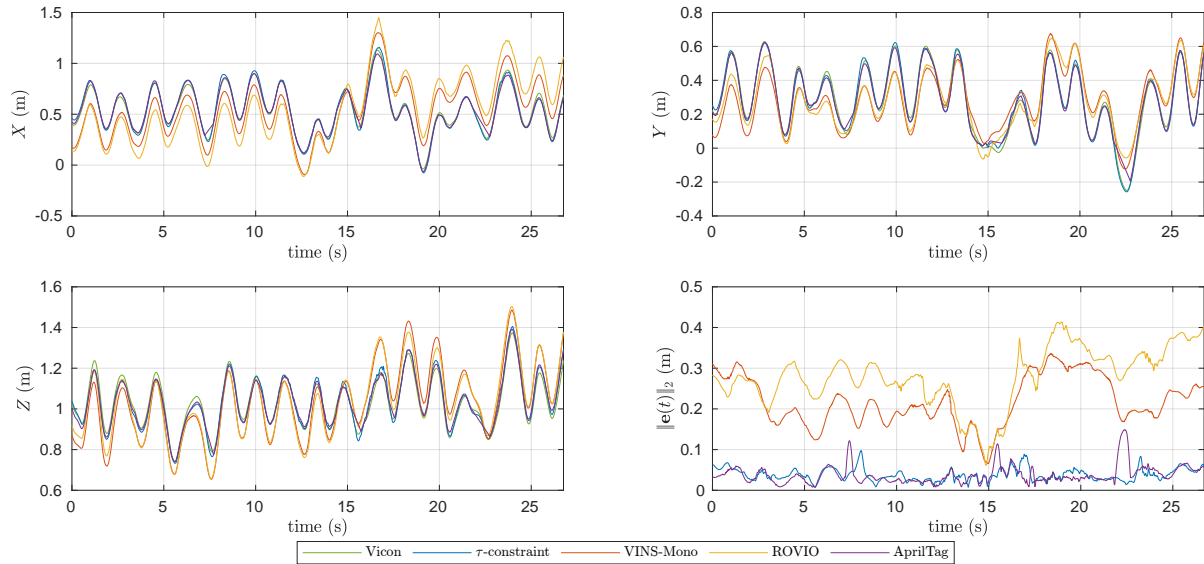


Figure 23. Sequence 9 estimated trajectories versus Vicon ground truth for all available estimation methods. All trajectories are aligned to the vicon by a rigid body transformation. (top-left) X axis trajectory, (top-right) Y axis trajectory, (bottom-left) Z axis trajectory, (bottom-right) l_2 error between estimated trajectories and Vicon ground truth.



Figure 24. Four representative frames from Sequence 10. The tracked patch is indicated by the white box. This sequence does not contain an AprilTag.

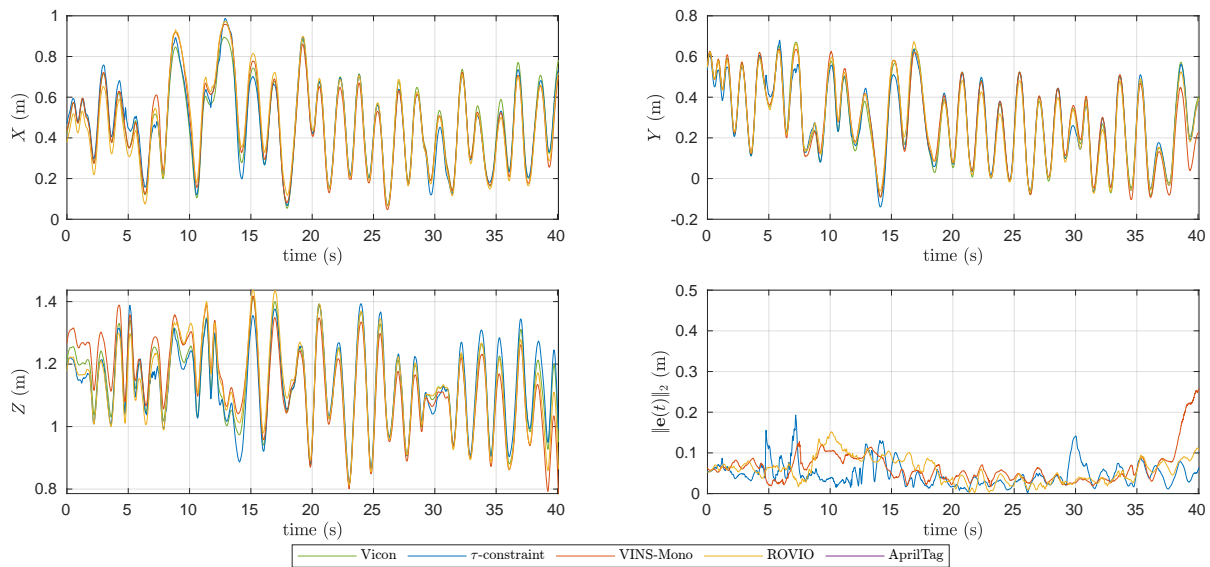


Figure 25. Sequence 10 estimated trajectories versus Vicon ground truth for all available estimation methods. All trajectories are aligned to the vicon by a rigid body transformation. (top-left) X axis trajectory, (top-right) Y axis trajectory, (bottom-left) Z axis trajectory, (bottom-right) l_2 error between estimated trajectories and Vicon ground truth.